Hugo
Guilherme Trigo

Estudo de precipitados ricos em Cobalto na liga de memória de forma Co – Ni – Ga

Study of Cobalt-rich precipitates in Co – Ni – Ga Shape Memory Alloy

Universidade de Aveiro
2022

Hugo Guilherme Trigo

Estudo de precipitados ricos em Cobalto na liga de memória de forma Co−Ni−Ga

Study of Cobalt-rich precipitates in Co−Ni−Ga Shape Memory Alloy

Dissertação apresentada à Universidade de Aveiro para cumprimento dos requisitos necessários à obtenção do grau de Mestre em Engenharia Física, realizada sob a orientação científica do Doutor João Cunha de Sequeira Amaral, Investigador Auxiliar do Departamento de Física da Universidade de Aveiro, e do Professor Doutor Oliver Gutfleisch, Professor Catedrático do grupo de investigação Funktionale Materialien da Technische Universität Darmstadt.

Texto Apoio financeiro do POCTI no âmbito do III Quadro Comunitário de Apoio.

Texto Apoio financeiro da FCT e do FSE no âmbito do III Quadro Comunitário de Apoio.

o júri

presidente

Professora Doutora Margarida Resende Vieira Facão
Professora Auxiliar do Departamento de Física da Universidade de Aveiro

vogais

Professor Doutor André Miguel Trindade Pereira
Professor Auxiliar da Faculdade de Ciências da Universidade do Porto

Doutor João Cunha de Sequeira Amaral
Investigador Auxiliar do Departamento de Física da Universidade de Aveiro

agradecimentos

Ao Professor Doutor Oliver Gutfleisch pela oportunidade que me proporcionou em realizar a minha tese no seu grupo de investigação, Funktionale Materialien.
À Doutora Franziska Scheibel por todo o apoio durante a minha estadia em Darmstadt e pela orientação científica prestada, sem a qual esta tese não seria a mesma, e ainda pela paciência em responder às minhas variadas "quick questions" durante o dia. A todo o restante grupo FM, pela ajuda nas formações, nas minhas questões sobre preparação de amostras, na minha integração, e pelos bons momentos de conversa vívidos em viagens de almoço ao Mensa.
Ao Doutor João Amaral por todo o apoio, científico e não científico, ao longo desta tese e destes últimos anos, que me ajudou muito a ultrapassar as minhas limitações e a crescer como pessoa e no mundo científico. Ao Doutor Carlos Amorim pela sua ajuda e contributo na minha orientação científica, pela paciência ao me explicar os conceitos importantes e por todos os bons momentos de conversa que tivemos no laboratório.
Por último, mas não menos importante, quero agradecer a todos os meus amigos e família pelas dores de cabeça, pelos momentos fora de casa, pelas ausências, e pelo apoio constante que me deram nestes anos da minha vida. Em especial à Rute, por todo o apoio, carinho e paciência.
Um grande Obrigado a todos.

Palavras Chave

Ligas com efeito de memória de forma, Precipitados, Caracterização Magnética, Ligas com Efeito de Memória de Forma a Altas Temperaturas, Transformação Martensitica, Tratamentos Térmicos, Microscopia Eletrónica, Microestrutura.

Resumo

A liga Co−Ni−Ga é um Heusler ferromagnético e com efeito de memória de forma a altas temperaturas, que demonstra bons efeitos de memória de forma e superelasticidade. O ajuste da histerese térmica, o intervalo de temperaturas e os efeitos de memória pode ser feito através da alteração da composição, da microestrutura, e/ou do controlo do crescimento dos precipitados pela escolha adequada dos tratamentos térmicos. É conhecido que os precipitados que se formam variam de forma, tamanho e número, com base na composição inicial da liga e dos tratamentos térmicos que são feitos. Eles podem precipitar como fase γ ou γ'. A fase γ tem uma estrutura $\mathrm{A1}$, maior concentração de Co, providencia ductilidade à liga, pode precipitar na fronteira de grão ou dentro dos grãos, e chega a ter o tamanho de vários microns. A fase γ' tem uma estrutura $\mathrm{L1_2}$, também uma maior concentração de Co, ajuda a fortalecer a matriz, precipita dentro dos grãos, e tem um tamanho mais pequeno, da ordem dos nanometros. Por causa da maior concentração de Co estes precipitados são ferromagnéticos. Como estes precipitados têm um impacto significativo nas propriedades de memória de forma da liga, a sua caracterização costuma utilizar High-Resolution Scanning Electron Microscopy (HR-SEM) ou Transmission Electron Microscopy (TEM), que são técnicas intensivas em termos de recursos e trabalho de preparação. Como tal, um método mais fácil para caracterizar é desejado pela comunidade científica. Neste trabalho, essa alternativa é apresentada. Primeiro, são tiradas imagens SEM que são depois tratadas para se obter uma indicação da quantidade de precipitados que estão a ser formados. Depois, caracterização magnética é feita para se ter uma ideia do impacto dos precipitados nas temperaturas de transição de fase, na saturação magnética e na histerese. É confirmado de que um aumento de precipitados diminui as temperaturas de transição, não afeta de forma significativa os valores da saturação magnética, e apresenta um comportamento complexo nas áreas de histerese. Apesar desta informação ser relevante em saber que existem precipitados formados, não apresenta uma correlação clara da quantidade de precipitados que estão a ser formados. Por consequência, a Lei da Aproximação à Saturação, um modelo fenomenológico, é aplicado e testado, mostrando resultados promissores para uma correlação com a quantidade de precipitados, o que significa que pode ser uma alternativa viável para uma quantificação mais fácil dos que os métodos atuais.

Keywords

Shape Memory Alloys, Precipitates, Magnetic Characterization, High Temperature Shape Memory Alloys, Martensitic Transformation, Heat Treatments, Electron Microscopy, Microstructure.

Abstract

Co−Ni−Ga alloy is a Heusler type ferromagnetic material and High Temperature Shape Memory Alloy that demonstrates good shape memory and superelasticity effects, even at high temperatures. The fine tuning of thermal hysteresis, temperature range and shape memory effects can be done by adjusting composition, changing the microstructure, and/or controlling the growth of precipitates with adequate heat treatments. The precipitates that are formed are known to heavily vary on shape, size and number, based on the composition of the initial alloy and the heat treatment that is done. They can precipitate as γ or γ' phase. The γ phase has a $\mathrm{A1}$ structure, higher Co content, provides ductility to the alloy, it can precipitate in the grain boundary and inside the grains, and can be as big as few microns. The γ' phase has a $\mathrm{L1_2}$ structure, also a higher Co content, helps strengthen the matrix, it precipitates inside the grains, and has a smaller, nanometric, size than the γ phase. Due to their high Co content, they are ferromagnetic. As these precipitates have a significant impact on the shape memory properties of the alloy, their characterization usually requires High-Resolution Scanning Electron Microscopy (HR-SEM) or Transmission Electron Microscopy (TEM), which is resource and labour intensive. Therefore, an easier method to characterize is sought after by the scientific community. In this work, such alternative is presented. First, SEM images are taken and treated to have an indication of the amount of precipitates that are forming for different heat treatments. Then, magnetic characterization is used to have an idea of the impact of the precipitates on the phase transition temperatures, the saturation magnetizations and the hysteresis. It is confirmed that an increase in precipitates lowers the phase transitions temperatures, it doesn't negligibly affect the saturation magnetization values, and it presents a complex behaviour in terms of hysteresis areas. Although this information is useful for knowing the presence of precipitates and the overall magnetic characteristic of the material, it does not present a clear correlation to the amount of precipitates that are being formed. As a result, the Law of Approach to Saturation, a phenomenological model, is applied and tested, showing promising results for the correlation to the amount of precipitates, which means that it could be a viable option for an easier quantification to the current methods.

Contents

List of Figures

List of Tables

Nomenclature

SMA	Shape Memory Alloy
SME	Shape Memory Effect
SE	Superelasticity
MT	Martensitic Transformation
TEM	Transmission Electron Microscopy
SEM	Scanning Electron Microscopy
BSE	Backscattered Electrons
EDX	Energy Dispersive X-Ray Spectroscopy
M_s	Martensite Start
M_f	Martensite Finish
A_s	Austenite Start
A_f	Austenite Finish
MFIS	Magnetic Field Induced Strain
FMSMA	Ferromagnetic Shape Memory Alloy
MSMA	Magnetic Shape Memory Alloy
HTSMA	High Temperature Shape Memory Alloy
FCC	Face Centered Cubic
BCC	Body Centered Cubic
WQ	water quenched
e/a	ratio of the average number of electrons per atom
DSC	Differential Scanning Calorimetry
T_C	Curie Temperature
MPMS3	Magnetic Property Measurement System 3
SQUID	Superconducting Quantum Interference Device
VSM	Vibrating Sample Magnetometer
GICM	Geometry Independent Correction Method
$M(T)$	Magnetization in Function of Temperature
$M(H)$	Magnetization in Function of Field

CHAPTER 1

Introduction

1.1 Shape Memory Alloys

Shape Memory Alloys (SMAs) are a class of multifunctional materials that have given interesting puzzles to researchers for the last several decades. Due to several unique properties as Shape Memory Effect (SME) and Superelasticity (SE), they have a wide range of applications on fields such as aerospace, automotive, biomedicine, manufacturing, energy exploration, sensors and actuators [1–3]. They can simplify, reduce and limit the wear and tear of complex multipieces designs, while adding sensing and actuation functions [4].

For most alloys used on everyday life, some of the factors that can be engineered for a specific purpose usually involve addressing the mechanical, thermal and/or electrical properties. However, if the alloy presents additional engineering functionality such as, sensing, actuation, electromagnetic shielding, etc., we have a multifunctional material. Shape memory materials fall under a subgroup of multifunctional materials called active materials. Due to their unique effects, these alloys exhibit a mechanical response when subjected to a non-mechanical field, which can be one or more orders of magnitude greater than the thermal expansion on regular materials. The coupling between mechanical and non-mechanical fields can be direct, if for a given input we get an output which is reversible. Otherwise there is a one way direction, known as indirect coupling. These kinds of couplings can be used for sensing or actuation properties of these materials [4].

The fundamental process that allows the existence of SMAs is the Martensitic Transformation (MT), which happens when a high temperature phase, usually called Austenite, transitions to a lower temperature phase, called Martensite. It was in 1963, when a group of engineers noticed a shape recovery capability on a Ni−Ti alloy used for heat shielding, that the MT was truly used as the basis for the effects present on SMAs [5].

As previously mentioned, the MT is a very well known and studied phase transition that happens between a parent phase, which is the high temperature phase, and a product phase, which is the lower temperature phase. The high temperature phase, Austenite, exhibits a

cubic structure. The product phase, Martensite, exhibits a lower symmetry phase such as orthorhombic, monoclinic [6], or tetragonal [7, 8].

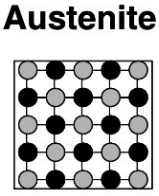

Figure 1.1: Austenite Schematic. Figure adapted from [4].

While the material is in the Austenite phase and the temperature is lowered, at a specific temperature, a change in the crystal structure happens and the formation of martensite starts. This temperature is known as M_s. This transformation is a first order transformation that occurs by a shear lattice distortion where there is no diffusion of atoms, but a coordinated rearrangement of these atoms in a new crystal structure. The transformation happens by nucleation and growth up until the M_f temperature, and since there is a lattice distortion, large strains are introduced, but can be reduced by two mechanisms: twins, and slips [9].

Twins are usually the most common deformations introduced in most alloys and are characterized by two different mirrored directions of Martensite next to each other, forming a twin boundary, and repeating this arrangement in the material. The two different directions are called Martensite variants. If the combination of variants results in a self-accomodation shape, where the change in volume is negligible, there is a formation of twinned martensite, figure 1.2a. When a specific orientation is dominant, usually induced by stress or other activation factors such as a magnetic field, it results in a shape deformation and detwinned martensite, 1.2b. Now, if the material is heated up, while in the martensite phase, at some point it will revert back to the austenite phase, called the A_s temperature, thus having a reverse transformation.

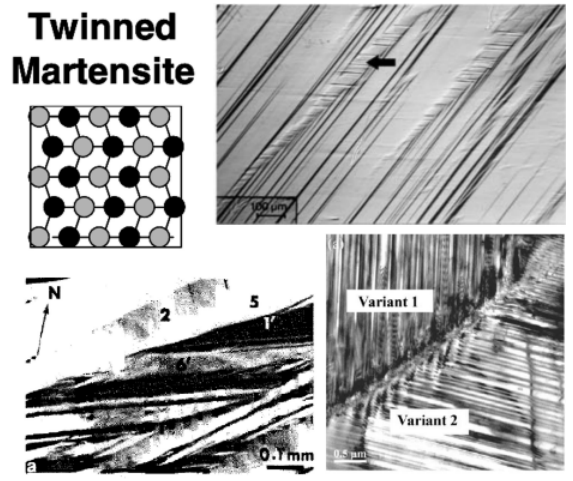

(a) On the top left corner there is a schematic of the twinned martensite, adapted from [4]. On the top right corner the black arrow points to internally-twinned martensitic plates, adapted from [10]. The bottom left corner shows a optical image of several martensitic variants, adapted from [9]. On the bottom right corner it is shown the Transmission Electron Microscopy (TEM) image of a interface between to martensitic variants, adapted from [11].

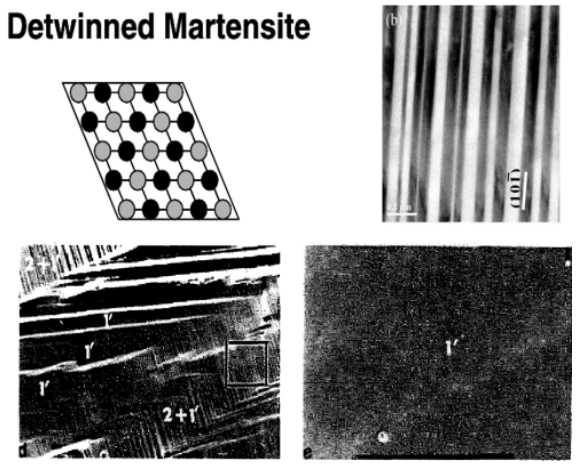

(b) On the top left corner there is a schematic of the detwinned martensite, adapted from [4]. On the top right is the morphology of a TEM image of one martensitic variant, adapted from [11]. The bottom images from left to righ show the progression of the detwinning process, where it has some variants, but enough stress causes it for to be one dominant variant, adapted from [9].

Figure 1.2: Schematic and examples of twinned and detwinned martensite.

The SME is a cycle where, starting in the austenite phase, the temperature is lowered until it reaches the twinned martensite state. Then, a stress induced in the martensite leads to de-twinning, and therefore a shape change. Once the stress field is removed, the martensite stays in detwinned mode and increasing the temperature changes the state to the original austenite. This cycle is the basis of many applications of the SMAs. In the case of SE, stress is applied directly to the austenite phase, causing it to change directly to detwinned martensite. Removing the stress makes the alloy go back to the austenite phase. Thus having a large shape change, but also recovery of the original shape. Both these cycles are drawn in figure 1.3.

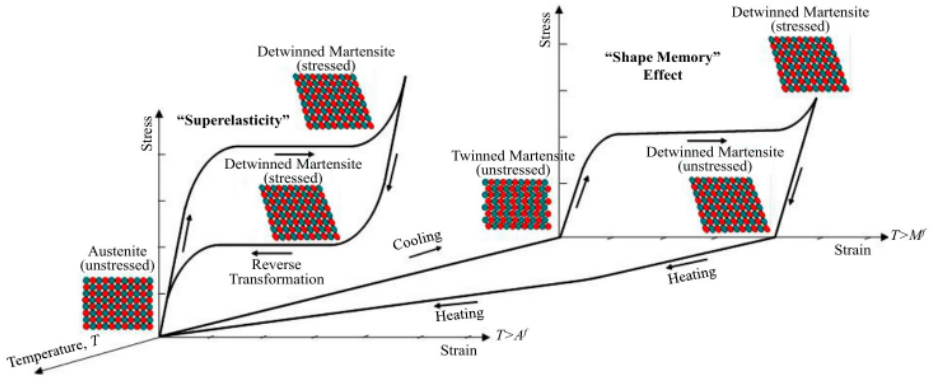

Figure 1.3: Diagram of the cycles exhibiting SE and SME. Figure extracted from [12].

1.1.1 Ferromagnetic Shape Memory Alloys

When it comes to the pratical application of the SME, a common shortcoming is the actuation or sensing speed. Even though large strains are attainable, the speed at which most SMAs work is limited by heat transfer which is not fast enough for most applications. Alloys that exhibit SME under the influence of a magnetic field solve this issue, and are often called Ferromagnetic Shape Memory Alloys (FMSMAs), but can also be referred to as Magnetic Shape Memory Alloy (MSMA). This effect comes from the magnetic-field-induced reorientation of the martensitic variants [4, 13], which is called Magnetic Field Induced Strain (MFIS). When compared to regular SMAs, FMSMAs show higher frequency of activation, as it is possible to see in the figure 1.4. Making them good choices for applications where speed of sensing or actuation is important.

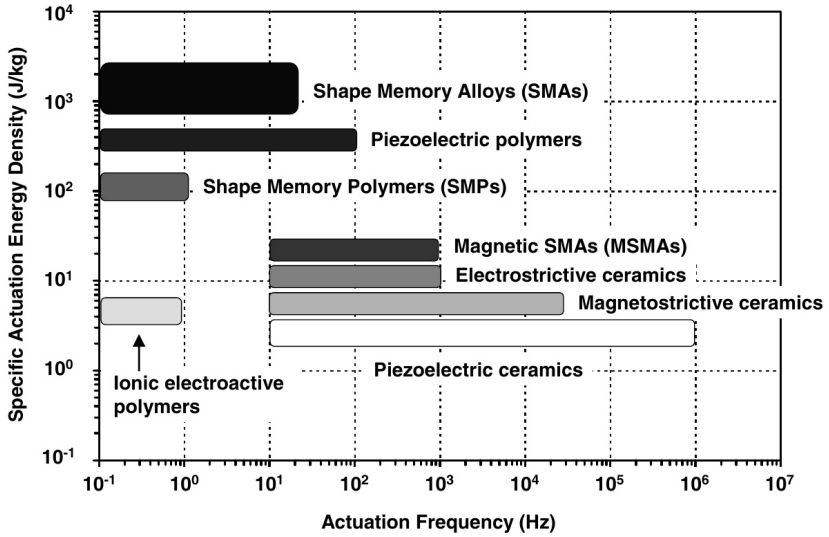

Figure 1.4: Diagram of the actuation frequency of the different active materials that exhibit direct coupling. Figure extracted from [4].

1.1.2 High Temperature Shape Memory Alloys

An aspect that is important when considering the application of a specific SMA is at what temperature the MT occurs. This is an important consideration that has to be taken into account in order to the SMA exhibit long term stability and ensure operation. Most MTs happen at cryogenic and environmental temperatures where diffusion processes, that can alter chemical and structural composition of the alloys, do not happen and thus ensuring high reversibility during the transformation. Diffusion processes such as decomposition, recrystallization, recovery, etc. happen at higher temperatures limiting the possible industrial applications in the areas of robotic, automotive, aerospacial, and others [14]. For transition temperatures higher than 100 °C, the SMA are referred to as High Temperature Shape Memory Alloy (HTSMA). According to the temperature range their MT happens, they can belong to one of three groups: group I for temperatures in the range of 100− 400 °C; II for temperatures between 400− 700 °C; and group III for temperatures above 700 °C [15].

There are a lot of possible promising FMSMA and HTSMA with all sorts of variations of elements, compositions, heat treatments, casting techniques, etc.. Some of the alloys that have been researched over the years are mentioned next, with some relevant literature for further reading.

Co based alloys like Co−Ni−Al [16] and Co−Ni−Ga [6] are presented as alternatives to Ni−Mn−Ga, due to their improved ductily and better SMEs [15, 17].

In the case of the Co−Ni−Al alloy, it started first as a binary composition of Ni−Al. This alloy family shows transformation temperatures that can go up to 900 °C, with high melting temperature and good resistance to oxidation, but are hindered by their ductility [18]. However, when Co is added to the alloy, there will be low temperature ductility, high temperature creep strength and stability [10].

Ni-based alloys show great diversity with the amount of different elements they can form HTSMA and FMSMA, either binary or ternary alloys, and the amount of properties they can

exhibit. Alloys such as the first and commercially successful reported SMA, Nitinol (Ni–Ti), has been extensively studied, and has great biocompability [5, 19].

Ni–Mn–Ga shows a giant MFIS [20] and a MT temperature higher than 250 °C [21], but has a tendency for intergranular fracture. Then there are the different possible ternary compositions of Ni–Ti–X (with X being Pd, Au, Pt, Hf and Zr) which have also been studied, but present expensive elements that are not suitable for most commercial applications [14, 15, 17, 18].

Cu-based SMAs are prone to chemical instabilities at high temperatures, the only promising composition at those temperatures is the Cu–Al–Ni [17, 18]. At lower temperatures the Cu–Zn–Al and Cu–Al–Ni are two of the three most commercially important SMAs, while the other one is the previously mentioned Ni–Ti. In terms of overall performance and/or biocompability the latter is the preferred choice, but if the application does not require to be biocompatible and the cost of the material is not taken into account, then the other two alloys are the preferred choices [22].

1.2 The Co-Ni-Ga System

Co–Ni–Ga is a ferromagnetic Heusler type HTSMA that has been studied since 2001 [6, 23]. Alongside Co–Ni–Al, this system has been stated as a possible alternative to Ni–Mn–Ga alloys. Ni–Mn–Ga alloys have been extensively studied over the years, as they exhibit a giant MFIS in single crystal form of 6 to up to 10% [20, 24] and in layered martensite [25]. On the other hand, Co–Ni–Ga does not show great MFIS when compared to Ni–Mn–Ga [26], but has good SME and SE at higher temperatures [10]. They also show excellent thermal stability, but lack durability, as they are very brittle in polycrystalline form. Co–Ni–Ga and Co–Ni–Al also show a wide range of transition temperatures when compared to Ni–Mn–Ga [11, 23], are more stable by not having volatile elements, such as Mn, have cheaper elements [7], good hot-workability, good room temperature ductility, high strength, low density, high melting point, and good corrosion resistance [27].

The matrix phase of Co–Ni–Ga and Co–Ni–Al is referenced to as β-phase, which is a B2 structure [6, 10, 23]. There is also the possibility of a higher ordering of the phase, in which case it is called β', with a $L1_0$ structure [8, 23]. While the high temperature phase is usually Body Centered Cubic (BCC), the lower temperature phase can be orthorhomic, monoclinic [6], or tetragonal [7, 8].

Through careful chosen heat treatments and composition, it is possible to precipitate other phases in the matrix of the Co–Ni–Ga alloy. The two main types of phases that are possible to precipitate are the γ and γ' phases. The γ phase greatly improves the ductility of the alloy [11, 23, 28] and is Co-rich in its composition [28, 29]. It has a disordered A1 Face Centered Cubic (FCC) structure [10, 11], and, although it varies, it can have the size of a few micrometers. The γ' precipitates have an ordered $L1_2$ FCC structure [10, 11], and are considerable smaller with nanometric sizes. These precipitates are said to strengthen the matrix [30].

There is a threshold temperature limit that smooths and removes secondary phases. This type of heat treatment is used to homogenize a sample. The temperature of this heat treatment can vary from 1000 to 1200 °C, last from 30 minutes up to several hours, and are water quenched (WQ) [30–32] to have a faster cooling rate and thus supress the formation of the secondary phases [29]. However, heat treatments made below that threshold temperature are able to precipitate these secondary phases [23, 33]. The shape, size and morphology of the precipitates is also greatly influenced by the alloy composition and heat treatments. It was reported that a higher Ga content precipitates rod-like shape structure, a lower Ga content precipitates a Widmanstätten-like structure, and for a even lower Ga content a blocky-like structure is formed. And, depending on the heat treatment, the γ' precipitates can precipitate inside the γ phase or at the interface of $\beta - \gamma$ phases [11]. In single crystals, it has been found that heat treatments of 620 K precipitate the γ' phase in dense dispersions and with nanometric size [33].

The transition temperatures are very sensitive to composition, heat treatments, and as a consequence, precipitates. The MT is agreed to be a first order transition due to its magnetization change when it does the transition [23]. For a composition of $Co_{46}Ni_{27}Ga_{27}$ it is possible to have MT temperatures between 40 and 250 °C, depending on the heat treatment performed [29]. The electron concentration, given by the ratio of the average number of electrons per atom (e/a), is a ratio used by the SMA community to classify the different compositions of the same alloy [29], but it should be used as a guideline as it does not account for all the interactions, defects or other relevant variables that can influence the properties of the material. Using it as such, for a Ni−Mn−Ga alloy, the MT temperatures have been found to have a proportionality relationship [34].

The γ precipitates that form have been said to decrease the MT temperatures of the matrix, by taking the surrounding Co and by consequence lowering the e/a [17, 29]. The γ' precipitates are also reported to lower the MT temperatures, increase the temperature hysteresis and decrease the SME in single crystals [33, 35]. If the precipitates were oriented, the change in the previous characteristics would be reduced. This is because these precipitates strengthen the austenite matrix and allow an easier accommodation of martensite [30].

Another way to evaluate the characteristics in function of composition is to keep the Ni/Ga ratio constant and changing the amount of Co. In this instance it was reported that an increase on Co leads to a decrease in MT temperature [7] and an increase of T_C [8].

It was reported that the γ and γ' precipitates have a strong impact on the thermal hysteresis and that the γ' precipitates have the potential to enhance cyclic reversibility of MT [17].

When precipitating the γ' particles on a single crystal of $Co_{49}Ni_{21}Ga_{30}$, they have been shown to increase the thermal hysteresis and drastically interfere with the MT dynamics, presenting themselves as resistance to movement, widening the MT as it can be seen in figure 1.5b [33].

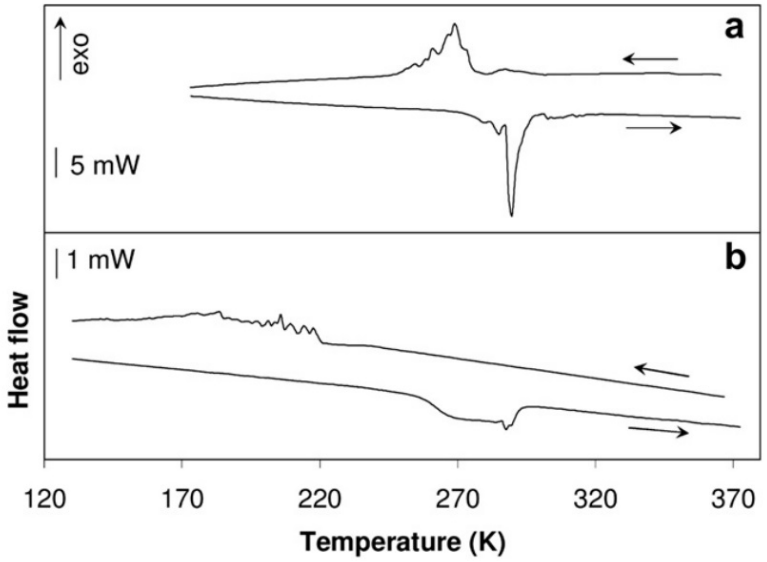

Figure 1.5: DSC thermograms of $Co_{49}Ni_{21}Ga_{30}$ alloy water quenched from (a) 1430 K and after a heat treatment of (b) 620 K for 1 hour. Figure extracted from [33].

Over the years, many different characterizations of the SME have been made. When it was first studied, a shape recovery of 67% of a 2% surface strain was possible. The reason for the incomplete shape recovery was attributed to the lack of recovery strain on the γ -phase [23], which coincides with the recommendation of avoiding the formation of the ductile second phase because it negatively impacts the SME and MFIS [11]. However, other results were also achieved. A complete shape recovery upon heating was observed between 20 to 60 °C [6]. In terms of pseudoelasticity, for the composition of $Co_{49}Ni_{21}Ga_{30}$ of a single crystal, the authors achieved a near perfect pseudoelastic behaviour with full strain recovery up until 400 °C, with the highest being a 4% between 60 to 140 °C, and lowest being $1,8\%$ at 400 °C [10]. The specific composition previously mentioned was chosen because is optimized for high recoverability with considerable formability, with very low precipitation of secondary phases such as γ and γ' [10, 11, 23]. The previous composition in single crystal state is also capable of rapid cyclic actuation frequencies of a few hundred Hz [27]. It was also found that Co−Ni−Ga exhibits a two-way shape memory effect in single crystals under a magnetic field [36]. Another way to prevent premature failure in polycrystalls is by changing the microstructure, as way to accomadate the volume shape change that happens at the MT [37].

It is known that composition and heat treatments also affect the saturation magnetization [6]. When an increase in Co was made, while keeping the Ni/Ga ratio constant, the saturation magnetization increased. However, it has been reported that the saturation magnetization does not have a good correlation with the e/a, so careful application of this ratio should be exercised [8].

As it was previously mentioned, the formation of the precipitates has a wide impact on the SMAs's MT, SME and SE properties. For that reason, a thorough understanding of these precipitates is needed and, currently, the only option is the usage of the SEM

and TEM techniques, which although being powerful and allowing for an almost complete characterization, are time and resource intensive. However, because the precipitates are magnetic, in this work, an alternative method that evaluates the presence of precipitates is presented that makes use of the magnetic characterization which is far simpler and quicker than the current alternatives.

CHAPTER 2

Methodology and Theoretical Concepts

2.1 Sample Preparation

In this work, a polycrystalline sample of Co–Ni–Ga SMA was used. Several ingots with the nominal chemical composition of 49 % Co, 21 % Ni and 30 % Ga (in at.%), were produced by vacuum induction melting [38], by Sophisticated Alloys (US) and provided in the as-cast condition by Dr. Christian Lauhoff, Dr. Philipp Krooß and Dr. Thomas Niendorf from University of Kassel. Then the ingots were cut in a diamond wire saw, figure 2.1b, and encased in quartz ampoules, figure 2.1c, in Ar atmosphere to do the various heat treatments. The initial state of the ingots showed an oxidation layer, as it is possible to see on the left of figure 2.1a. After the heat treatment, this oxide layer was removed via hand polishing, and a small rectangular cuboid was cut to be used on the magnetic characterization, while the rest was used on the SEM.

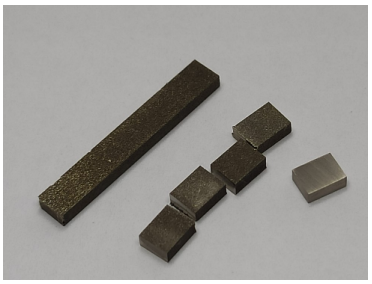

(a) Example of a ingot, on the left, cut into four pieces and then polished.

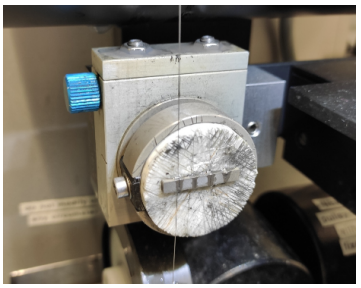

(b) Wire saw cutting of the ingots. The bonding between the polycrystalline sample and the wire saw was done using crystal bonding.

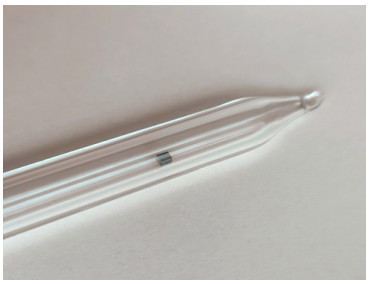

(c) Encapsulation of a single piece inside a quartz ampoule in Ar atmosphere for heat treatment.

Figure 2.1: Images of the processes used during the sample preparation

The heat treatment was done on a Carbolite Gero Tube Furnace with temperature control,

and the samples were quenched in a bucket of water immediately after being taken out from the furnace. The times and temperatures done on the As-Cast state are present in table 2.1.

Table 2.1: Annealed Samples of the As-Cast material

Sample Number	**Ann. Temp. (°C)**	**Ann. Time (hours)**
FM10034	No annealing	No time
FM10035	400	1.0
FM10095	450	1.0
FM10036	500	1.0
FM10071	500	1.5
FM10050	500	2.0
FM10051	500	3.0
FM10070	500	4.0
FM10096	550	1.0
FM10037	600	1.0
FM10072	600	2.0

2.2 Imaging and Precipitates Characterization

2.2.1 Scanning Electron Microscopy

In order to use the SEM, the pieces were first encased in Tecnovit ® 5000, under pressure to remove bubbles. Then each of the different pucks, embedded with different samples, were polished by hand with an increase of the grit of sandpaper up to 4000, followed by several diamond particles with sizes of 3 to 1 µm suspended in an ethanol based liquid and then finished with Oxide polishing solution. The microscope used was the JEOL JSM-7600F Schottky Field Emission Scanning Electron Microscope [39]. Because the focus it is not on the topography of the material, but in the distinction between different phases. The images were collected by Backscattered Electrons (BSE) detection. An example is shown in figure 2.2, where several BSE images, with different magnifications of the As-Cast sample, are present. All the SEM images for the other heat treatments are in Appendix A - Scanning Electron Imaging.

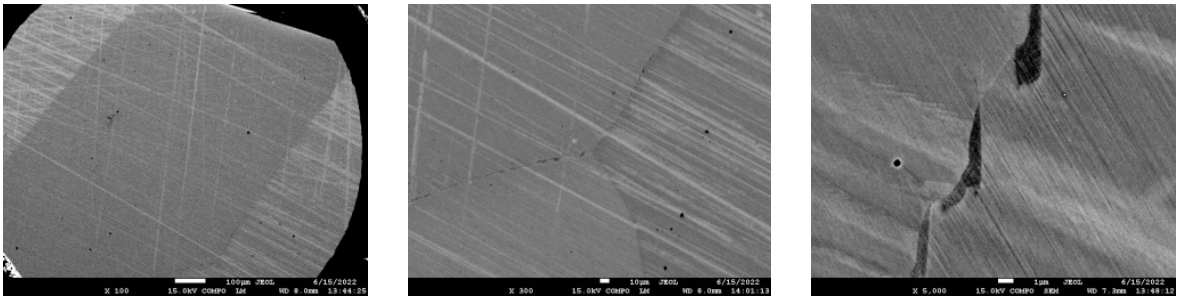

(a) Amplification of 100x. **(b)** Amplification of 300x. **(c)** Amplification of 5000x.

Figure 2.2: SEM images of the As-Cast sample.

2.2.2 Precipitates Analysis

To have a quantitative answer about the number of precipitates that are being formed, a method based on the ImageJ software and MatLab was used. Due to the moderate quality of the images due to artefacts, noise, scratches and other defects, the following method relies on the eye and best judgement of the person using it. However, the method also accounts for this human introduced error.

First, a representative area with precipitates was used, figure 2.3b. Then, using the imageJ software, the noise of the image was reduced and the contrast enhanced in order to have a "baseline" image, figure 2.3c.

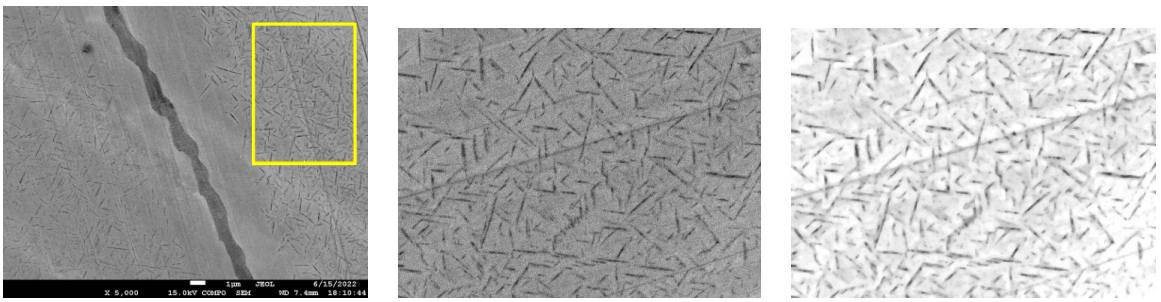

(a) Area selection.

(b) Baseline image before any type of image treatment.

(c) Baseline image after the image treatment for noise and contrast.

Figure 2.3: Choice of representative area of the precipitates in the 2 hours at 500 °C sample and consequent noise treatment for further analysis.

From this "baseline" image three other images were produced using the threshold function that makes the images black and white. In one of them the threshold of black and white was adjusted in such a way that underselects the precipitates, figure 2.4a, another one adjust for the "best guess", figure 2.4b and the last one overselects the precipitates, figure 2.4c. After that, all the images were again treated for noise, and points that were not precipitates were erased. The outline of this process for each of the heat treatments that produced precipitates is present in Appendix B - Precipitates Analysis. For some of the heat treatments, where the image quality was poor, several areas were selected and this process was applied to all of them. Later, the values obtained were averaged to estimate a single number.

(a) Threshold of the baseline image adjusted for an underselection of the precipitates.

(b) Threshold of the baseline image adjusted for a "best guess" of the precipitates.

(c) Threshold of the baseline image adjusted for an overselection of the precipitates.

Figure 2.4: Three different threshold adjustments for the precipitates analysis of the 2 hours at 500 °C sample.

Once the black and white images are produced, a simple algorithm in MatLab counts the black pixels and divides them by the total pixels of the images, resulting in a value that represents the area of the precipitates produced. For example, in the case of the 2 hours at 500 °C sample demonstrated before, the underselection resulted in a value of $4,98\,\%$, the "best guess" in $9,42\,\%$ and the overselection in $14,94\,\%$.

2.3 Magnetic Characterization

The measurement of the magnetic properties was done by the commercial MPMS3 magnetometer, built by Quantum Design [40]. A popular device that is versatile and allows automation of the sequences used for the measurement of magnetic moments, and other properties, with very high sensitivity [41]. They are based on a Superconducting Quantum Interference Device (SQUID) which is the most sensitive magnetic flux detector, with a field resolution up to 10^{-17} T [42]. The SQUID is coupled to a set of detection coils in a second order gradiometer configuration, figure 2.5a, that eliminates background noise whilst giving a good signal-to-noise ratio [42, 43].

Due to being such a sensitive device and the way it is constructed, some considerations must be taken into account in order to correctly measure the intended properties. The MPMS3 has small pick-up coils, assumes every sample to be a point like magnetic dipole and it measures the magnetic field lines that arise from the sample. A known shape will facilitate the correction of geometrical errors and careful positioning of the sample will reduce the radial offset error. An example of the mounting is present on figure 2.5b. Nevertheless, geometrical errors will always be present. So a correction method independent from the geometry of the sample was used, called GICM [44]. To use this method, the magnetic moment of the sample must be measured both in the DC-scan length and Vibrating Sample Magnetometer (VSM) modes once at saturation. The only measurements that were corrected, using this method, were the ones performed as a function of applied field at a fixed temperature. The third and last consideration was the trapped current inside the superconductive loop of the SQUID. The non existence of resistivity of this loop, means that there is always some previous trapped current from a measurement that can influence the measurement of the next sample. This is

specially important for samples measured at very low fields. To mitigate this problem, when initiating or finishing a measurement, an oscillatory change of the magnetic applied field to zero should be done. A resetting of the SQUID is also possible. In this case, the MPMS3 heats up the superconducting loop to a temperature where it stops being superconducting for a few moments and thus extinguishing the current, before coming back down again.

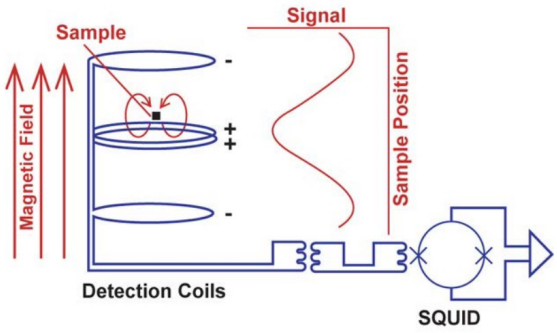

(a) SQUID detection schematic. Figure extracted from [43].

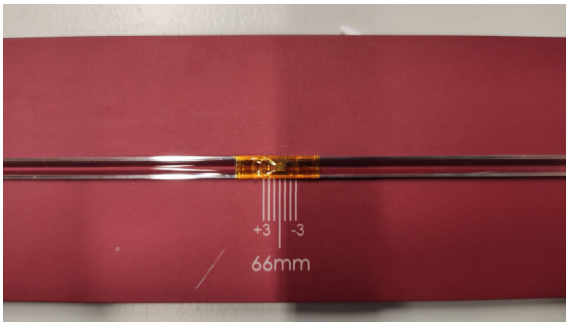

(b) Sample mounting on the quartz rod with kapton. The sample was carefully mounted in order to ensure the most attainable centering to reduce radial offset and vertical offset.

Figure 2.5: Schematic and sample preparation of the MPMS3.

2.3.1 Magnetization with field and temperature dependence

Two main types of measurements were done using the MPMS3, the Magnetization in Function of Temperature ($M(T)$) and Magnetization in Function of Field ($M(H)$). The $M(T)$ curves were measured in order to see the variations of the temperatures of the phase transitions such as M_s, M_f, A_s and A_f and T_C. This way, the $M(H)$ curves could also be put into perspective and know in what phase they were being measured. These $M(T)$ curves were measured from 15 K to 380 K with a constant applied field of $\approx 0,01$ T. As these samples were polycrystalline, a small applied field was necessary to align most of the magnetic moments, but still allow a significant change in magnetization when the material transitions to another phase. An example of this type of measurement made in the As-Cast sample is present in figure 2.6a, while a comparison to a heat treatment of 2 hours at 500 °C is present in figure 2.6b and the rest of the heat treatments are present in Appendix C - Magnetization with field and temperature dependence. In this brief example, for the As-Cast sample, it is possible to see that the T_C is around 367 K, the M_s is near the 254 K and M_f near the 211 K, while the A_s is around 236 K and the A_f is at 271 K. Contrasting with the previous example, the 2 hours at 500 °C sample is completely in the austenite phase and the T_C shifted to around 135 K.

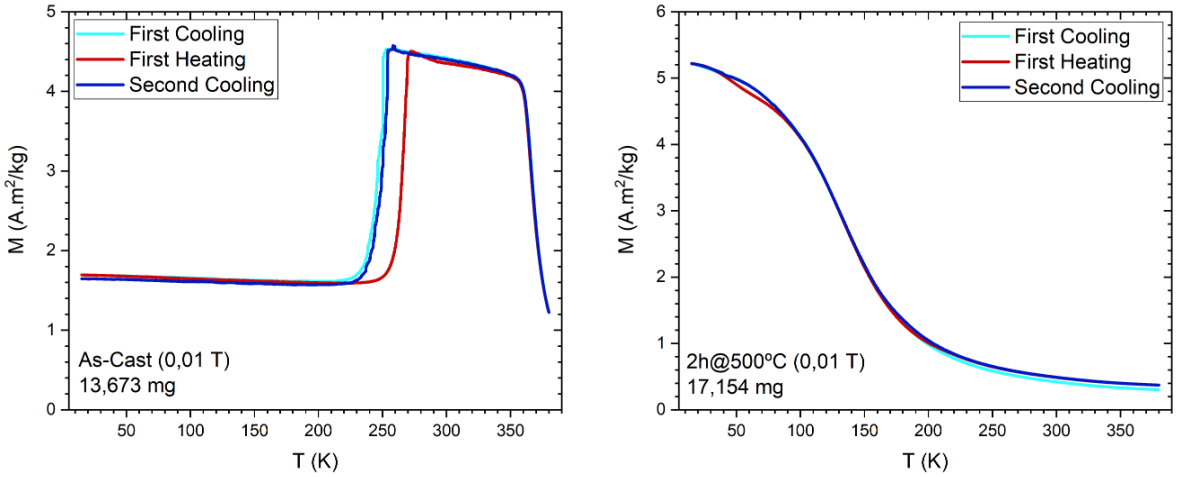

(a) $M(T)$ for the As-Cast with a mass of 13.673 mg. All the measurements made while cooling and heating had an applied field of $\approx 0,01$ T.

(b) $M(T)$ for the 2 hours at 500 °C with a mass of 17.154 mg. All the measurements made while cooling and heating had an applied field of $\approx 0,01$ T.

Figure 2.6: Comparison of the $M(T)$ of the As-Cast and 2 hours at 500 °C.

In order to have a complete magnetic characterization of a material, it is necessary to measure the magnetic hysteresis, as it gives information about coercivity, domain wall motion, defects, saturation and remanent magnetization, susceptibility, etc.. Two main sets of $M(H)$ curves were measured. The first set was a measurement that went from 2 to -2 and back to 2 T, as they were the points at which the sample was saturated, and they were done at four different temperatures. The first curve to be measured was at 100, followed by the 200, 300 and lastly 350 K. The choice of these temperatures was to measure all the different phases of the material. All the curves were corrected for geometry errors with the GICM [44]. An example of this type of measurement made in the As-Cast and 2 hours at 500 °C sample is present in figure 2.7. The rest of the heat treatments are present in Appendix C - Magnetization with field and temperature dependence.

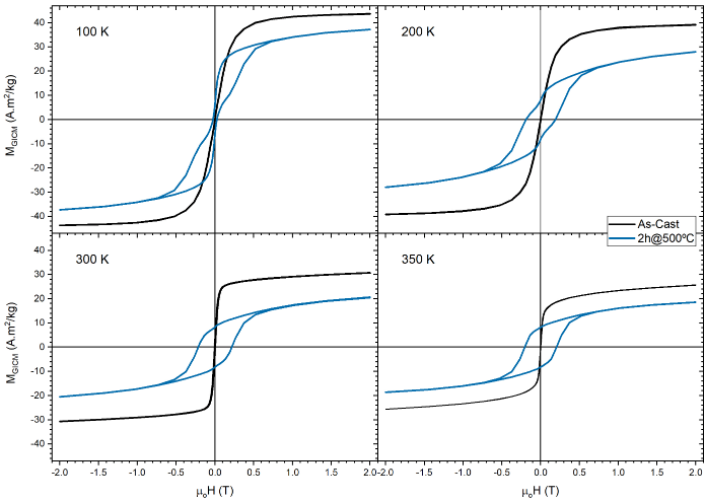

Figure 2.7: Magnetization in function of applied field for the As-Cast and 2 hours at 500 °C samples. Each magnetic cycle was measured at four different temperatures, namely, 100, 200, 300 and 350 K. The curves were corrected for geometry errors with the GICM [44].

The second set of $M(H)$ arises from the need of having a lower temperature, in this case 10 K, to reduce the impact of thermal fluctuations in the magnetization, and more points to be fitted to the Law of Approach to Saturation. More information about this law is given in the subsection 2.3.2. To achieve this goal, the measurement started, and was measured, this time from 0 emu magnetization by means of a previous oscillatory field. Then the magnetization was increased to 3 T and measured with small steps, resulting in a higher point density. Then the magnetization was further increased to 7 T, but this time with less points measured. Once it reached 7 T, the same process was applied backwards toward 3 T with fewer points, then from 3 T to $-0,1$ T, to also obtain the coercivity, with more points. As the hysteresis is a symmetric shape, there is no need to measure the negative magnetization, for that reason the field was only decreased to -7 T to have that symmetry, but without measurements. Once it reached -7 T, the field was, again without measuring, increased to $-0,1$ T and only after that did the measurement start to obtain the coercivity and the final magnetization curve. This curve went from $-0,1$ T to 3 T, with high point density, and then finished at 7 T, with lower point density. The result of this type of measurement is present for the As-Cast sample in figure 2.8a and for the 2 hours at 500 °C in figure 2.8b. The remaining heat treatments are present at the end of Appendix C - Magnetization with field and temperature dependence.

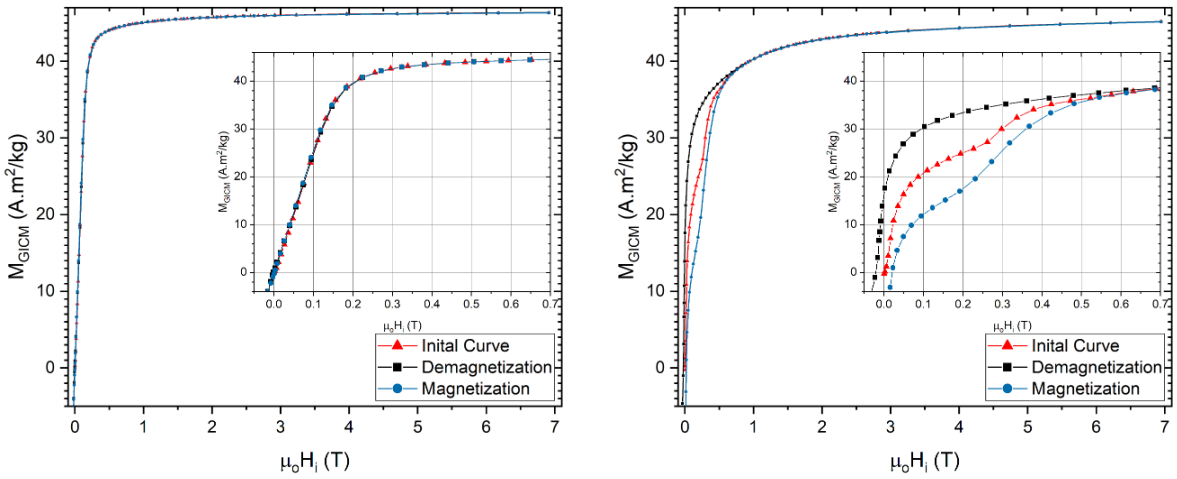

(a) Magnetization in function of applied field for the As-Cast sample at 10 K.

(b) Magnetization in function of applied field for the 2 hours at 500 °C sample at 10 K.

Figure 2.8: Comparison of the M(T) curves of the As-Cast and 2 hours at 500 °C sample.

2.3.2 Law of Approach to Saturation

In a possible attempt to gain a quantitative understanding of the impact of the precipitates on the magnetic properties, as it was previously mentioned, the Law of Approach to Saturation was fitted to the low temperature $M(H)$ curves. A brief explanation of the Law of Approach to saturation, adapted from [45], is made in this section, as well as an explanation of the fitting method.

The Law of Approach to Saturation assumes a large enough field applied to a material, where all possible wall displacements have already taken place and the magnetization, M, is found to be almost parallel to the applied field, thus being in a state of almost saturation, M_S.

$$M = M_S \cos\theta = M_S \left(1 - \frac{\theta^2}{2} + ...\right) \tag{2.1}$$

At this point, the torque that is trying to align the material's magnetic moment to the field and the torque that is applied by the magnetic anisotropy of the crystal, E_a, are balanced, as it is shown in the schematic of figure 2.9.

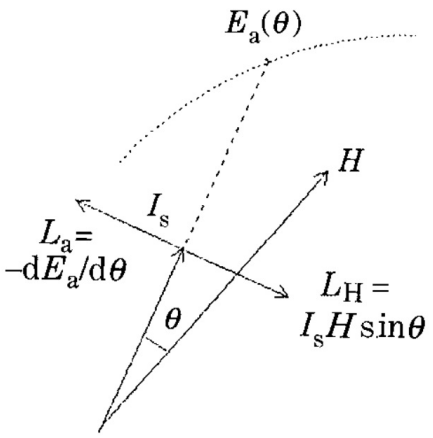

Figure 2.9: Rotation of magnetization against the magnetic anisotropy. Figure extracted from [45].

By equalling this and after some algebra, the result is the law of approach to saturation, empirically obtained (equation 2.2)

$$M = M_S \left(1 - \frac{A_1}{\sqrt{H}} - \frac{A_2}{H} - \frac{A_3}{H^2} - ...\right) + \chi_0 H \tag{2.2}$$

Each and every one of these terms are related to a certain type of mechanism that causes a deviation from the M_s. There is some debate as to what is the correct source that causes the deviation of each term, but in the literature it was found that the term $A_1/\sqrt{H}$ is attributed to the existence of the exchange interaction between ferromagnetic and antiferromagnetic clusters [46]. The term A_2/H is attributed to defects and impurities [46], structural defects or non-magnetic inclusions [47]. The term A_3/H^2 is attributed to crystal anisotropy [45, 47]. Lastly, the term χ_0 is attributed to the high-field susceptibility [45, 48].

In order to do the fitting, the first step taken was to evaluate which term had the biggest impact and necessary, and which was not. For that, several different equations were tested and the contribution of each term was plotted. In total, ten different combinations of terms were fitted and tested to evaluate these terms. Below, there are two examples of this process, where for equations 2.3 and 2.4, there is a corresponding plot of the contribution of each term for the As-Cast and 2 hours at 500 °C samples, in figures 2.10 and 2.11, respectively.

$$\frac{M(H_i)}{M_S} = 1 - \frac{A_1}{\sqrt{H_i}} - \frac{A_2}{H_i} - \frac{A_3}{H_i^2} + \frac{\chi_0}{M_S} H_i \tag{2.3}$$

$$\frac{M(H_i)}{M_S} = 1 - \frac{A_2}{H_i} + \frac{\chi_0}{M_S} H_i \tag{2.4}$$

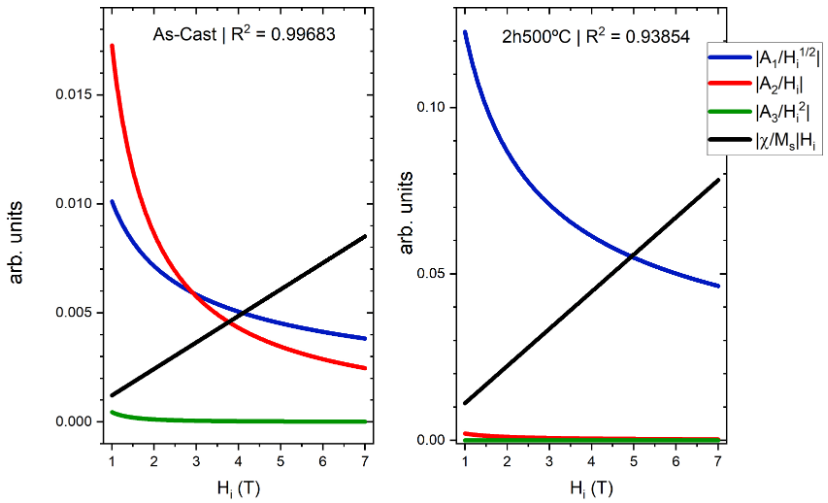

Figure 2.10: Contribution of each term on equation 2.3 on the As-Cast and 2 hours at 500 °C samples.

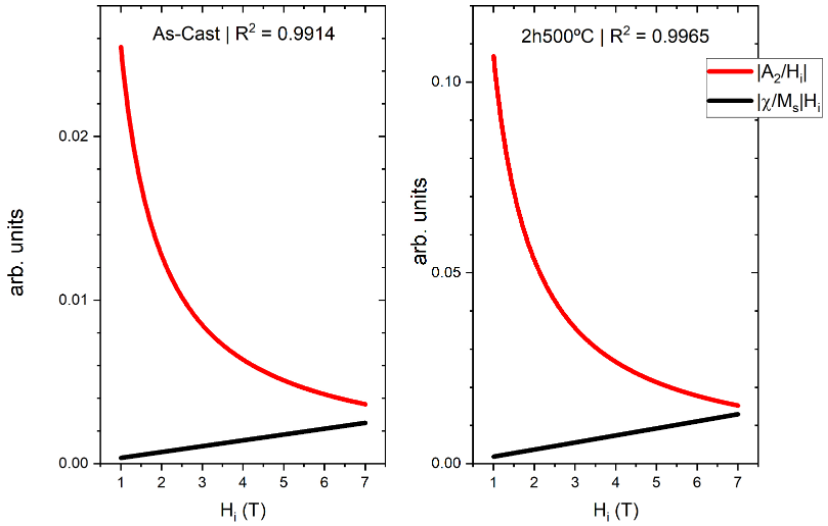

Figure 2.11: Contribution of each term on equation 2.4 on the As-Cast and 2 hours at 500 °C samples.

In each individual fit for a specific equation, the assessment of the quality of fit followed loosely the indication of the R^2, although for a more thorough fit, the residuals were evaluated on a case by case basis. This way, it was possible to visually ensure a higher quality fit and have a sense of what each term was doing, instead of relying only on the R^2, and thus having a systematic approach to test different equations. As an example, the As-Cast sample is fitted in figure 2.12a and the fit of the 2 hours at 500 °C sample is in figure 2.12b, using equation 2.4. Every fit that was done for equation 2.4, along with the residuals is present in Appendix D - Law of Approach to Saturation.

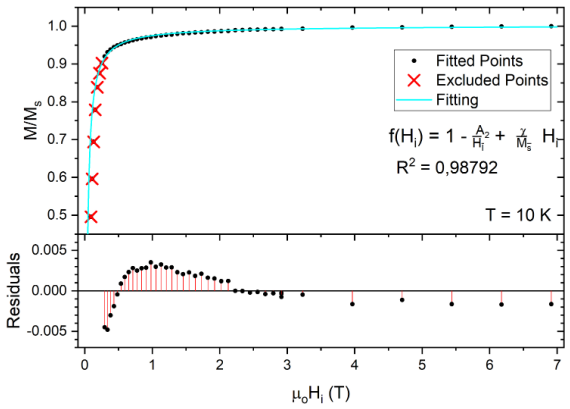

(a) Fitting of the As-Cast sample at 10 K.

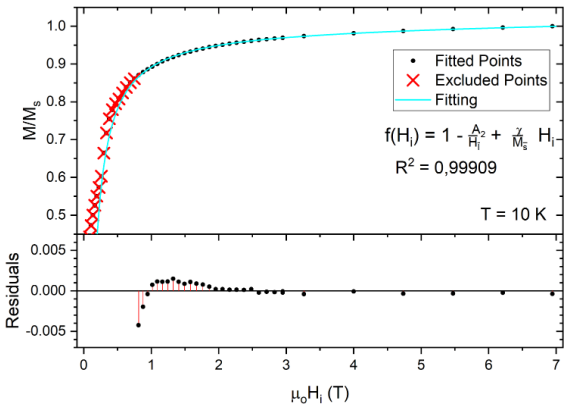

(b) Fitting of the 2 hours at 500 °C sample at 10 K.

Figure 2.12: Comparison of the fittings of the curves of the As-Cast and 2 hours at 500 °C sample.

CHAPTER 3

Results and Discussion

3.1 Microscopy Analysis from Precipitation formation

After using the method described in subsection 2.2.2 the fraction area of the precipitates is present in figure 3.1.

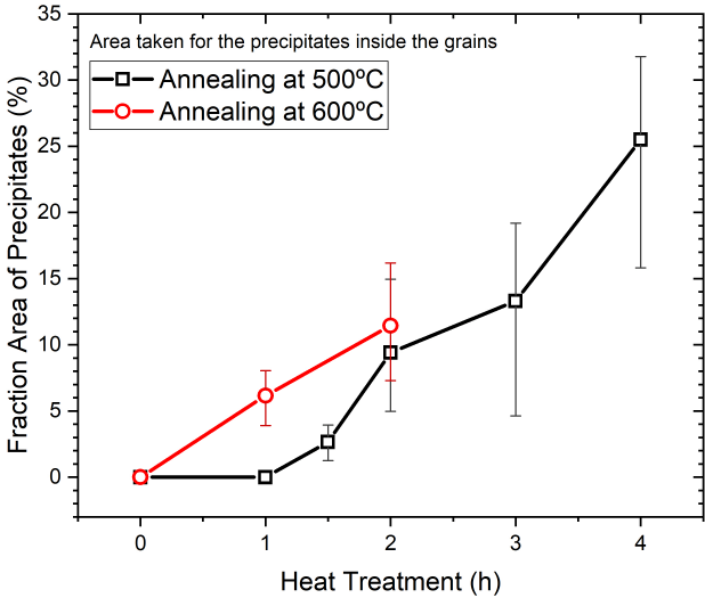

Figure 3.1: Fraction area of the precipitates caused by each heat treatment using the method described in subsection 2.2.2. The black line and squares are for the heat treatments at 500 °C in function of the time, and the red line and circles are for the 600 °C heat treatments.

In figure 3.1, there are the results of two different heat treatment temperatures, 500 °C and 600 °C, with a range of different times. These were the two temperature ranges that produce precipitates detected on the SEM. Nevertheless, as is the case for the 1 hour at 500 °C sample, it is possible to see precipitates, figure 3.2, but it is not possible to distinguish them from noise by the ImageJ method that was discussed in subsection 2.2.2.

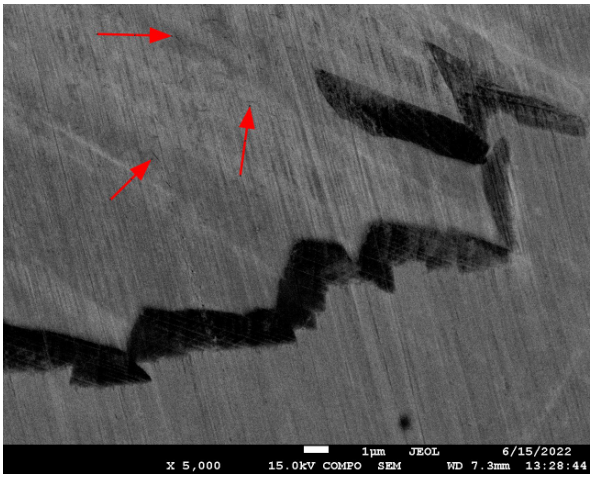

Figure 3.2: SEM image of the 1 hour at 500 °C sample with red arrows indicating precipitates. This image has been contrast enhanced.

Therefore, it is important to remember that other heat treatments most probably also have precipitates, but they are on a much smaller scale than the one that was possible to be measured on the SEM. This is because the γ' structures are said to precipitate in nanometric sizes, while the γ precipitates have considerable higher sizes [11, 30, 49]. Based on the previous statement, it is safe to assume that the precipitates that are being seen on the SEM images obtained are in the γ phase. Particularly at higher temperatures, there is formation and/or growing of a secondary phase at the grain boundary, which is a characteristic feature of the ductile γ phase in the Co–Ni–Ga alloy, figure 3.3. Through Energy Dispersive X-Ray Spectroscopy (EDX) analysis the grain boundary is known to have a higher Co percentage than the matrix, roughly 65 % (at.%) in comparison to the 48 % (at.%), respectively. The formation/growing of this phase on the grain boundary causes a depletion of Co in the neighbouring area, which translates to no precipitates formation in this region.

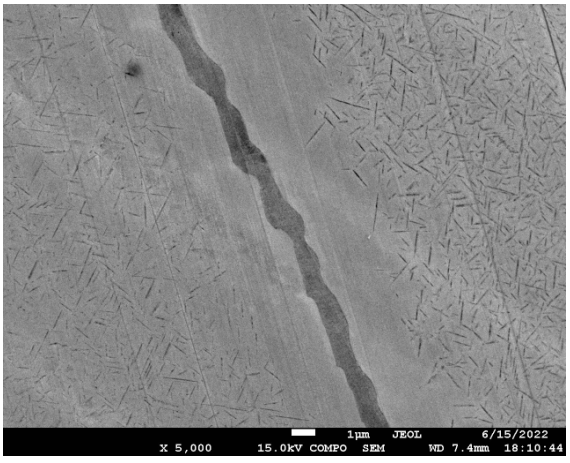

(a) SEM image of the 2 hours at 500 °C with the higher Co phase appearing darker.

(b) SEM image of the 1 hour at 600 °C with the higher Co phase appearing darker.

Figure 3.3: Comparison of SEM images in BSE mode.

From the graph in figure 3.1 it is possible to observe that higher annealing temperatures,

for the same time, have a higher growth of precipitates. As the time of heat treatment increases, so does the amount of precipitates, but the plateau of precipitate formation was not reached. This type of plateau was hypothesized to exist, due to the amount of Co that the precipitates can take from the matrix is finite.

Figure 3.1 is an indication of the precipitates formation. It serves as the basis comparison of this work, meaning it will be the graph to relate to when doing further measurements and characterizations. However, it is important to notice that previous study of the evolution of the γ phase were done, and, in the case of a phase volume, the results are lower than 20 % even at heat treatments made at 900 °C [49]. Considering this fact, it is important to put the result of the calculation of the area fraction into perspective and understand that it has a high degree of uncertainty and it does not present the whole picture about the precipitates formation.

3.2 Magnetic Characterization

3.2.1 Phase Transitions

Based on the $M(T)$ curves, the estimation of the different phase transitions and Curie temperatures was obtained. This information is present in figure 3.4.

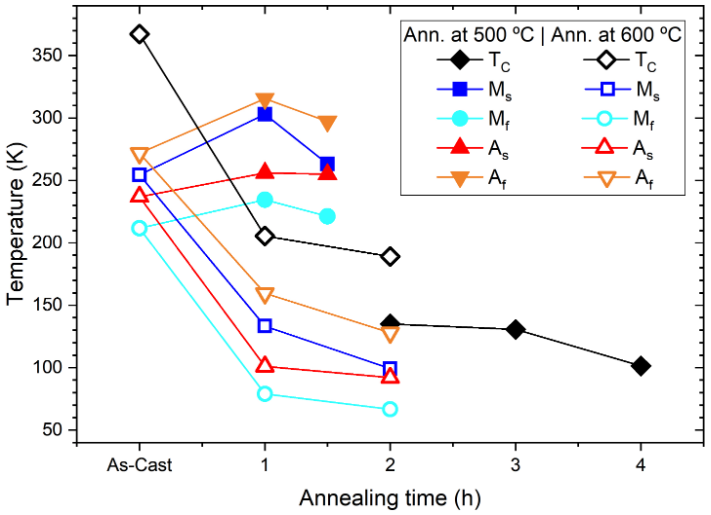

Figure 3.4: Estimation of the temperatures of the different phase transitions, M_s, M_f, A_s, A_f and T_C, for the two heat treatments of 500 °C and 600 °C in function of time.

From this figure there is not much information that could be useful to quantify the precipitates formation. At first glance the phase transition in the heat treatments made at 500 °C shows a behaviour that seems to be erratic. It first goes up, for the 1 hour at 500 °C sample, and then it goes down to the 1 hour and 30 min at 500 °C sample. After that it changes drastically and only the T_C temperatures could be obtained. At this point, there seems to be no change from austenite to martensite that could be measured. However, this is one of the problems encountered when looking at the phase transitions estimations using the $M(T)$ curves. At small fields, and with the growth of precipitates, the phase transitions

are smeared out and are not easy to estimate. One example of this is the 2 hours at 500 °C sample in figure 3.5a. In this case there is a very small change of magnetization, but there is no reliable way to know when it starts and when it finishes. One alternative to measure the phase transitions would be to use a DSC, but, even then, the transitions would be smeared out and the result would not be useful for the precipitates quantification. In contrast with this situation, for the same duration, but at a higher temperature of 600 °C, the phase transitions are easily seen in figure 3.5b.

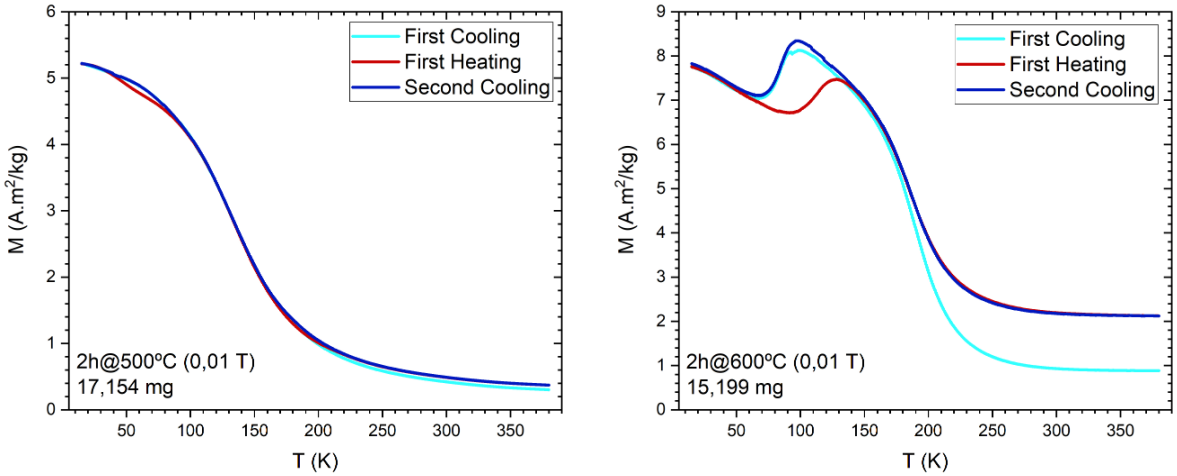

(a) $M(T)$ curves of the 2 hours at 500 °C sample. **(b)** $M(T)$ curves of the 2 hours at 600 °C sample.

Figure 3.5: Comparison of the $M(T)$ curves.

Returning to the phase transitions temperature behaviour, it is known that the formation of precipitates changes the composition of the matrix and this leads to a decrease of the MT temperatures [17, 29], as well as these precipitates resistance to the accommodation of the martensite, which is the effect seen for the heat treatments longer than 2 hours, that further decrease the MT temperatures [30]. Nevertheless, there is still no explanation to the initial increase of the MT temperatures. In this case, the formation of the precipitates is possible to be low enough to not resist the movement of the martensite twins, which are absorbed, and the chemical change that happens in the matrix leads to a very small, and unexpected, increase in MT temperatures. Because the precipitates formation is varied, it is possible that, up until that point, another type of precipitates is being precipitated. Nonetheless, the information gathered from the MT temperatures does not serve the purpose of having an indication of the amount of precipitates, but it contributes to the understanding of phase transformations of the different heat treatments.

3.2.2 Magnetic Saturation and Hysteresis

The next results used to compared to the precipitates formation were the saturation magnetizations of the samples at 10 K. At this point, the literature clearly states that there is Co going from the matrix to the precipitates. Both of their crystal structures are different, which could mean that the amount of precipitates could affect the saturation magnetization in such a way that the net magnetization would increase or decrease with the amount of

precipitates. This trend would probably allow to quantify of the amount of precipitates when compared to the figure obtained in 3.1. The saturation magnetization in function of the heat treatments duration is present in figure 3.6.

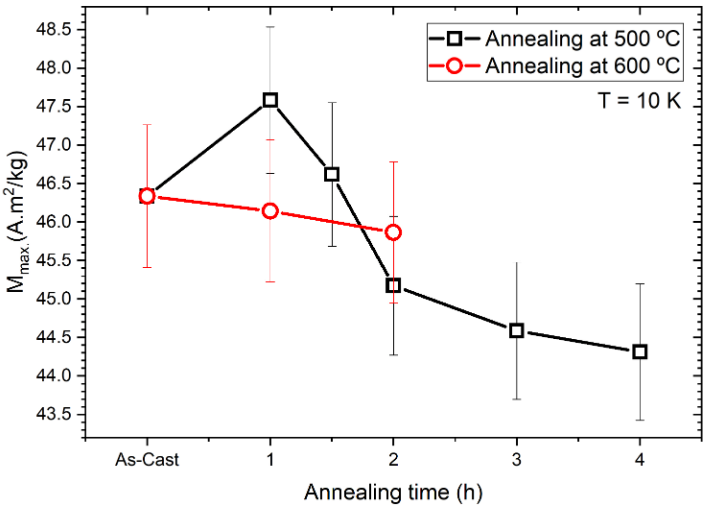

Figure 3.6: Saturation magnetization of the $M(H)$ curves measured at 10 K, for the different heat treatments.

On the 500 °C heat treatments, first it goes up with the heat treatment duration and then down, which is not what is encountered when looking at the progression of the formation of the precipitates. The saturation magnetization of the 600 °C heat treatment goes down immediately and it has a very nice trend that follows the trend of the precipitates formation. Regardless of these trends, is important to notice that these changes are very small, in the order of the uncertainty of the measurement, even when corrected with the GICM [44]. This is a step closer to the indication of the precipitate formation, but it still leaves doubts if it is reliable enough and if it can be used in other situations, mainly when different phases are being compared. For this reason, other attempts at looking for a property that can lead to the quantification of the precipitates, must be made.

When looking at the different hysteresis curves, it was found that depending on the heat treatment made, they vary significantly. Knowing that the hysteresis is a complex contribution of each of the phases and the matrix present, this was one of the approaches that looked promising towards the quantification of the precipitates formation. An example of this are the $M(H)$ curves of the samples 1 hour and 30 min at 500 °C, 2 hours at 500 °C and 2 hours at 600 °C, that are present in figure 3.7, where it is possible to see that even for the same time of 2 h, different temperatures produce different hysteresis shapes and areas. This also supports the idea that different precipitates are being formed when doing different heat treatments.

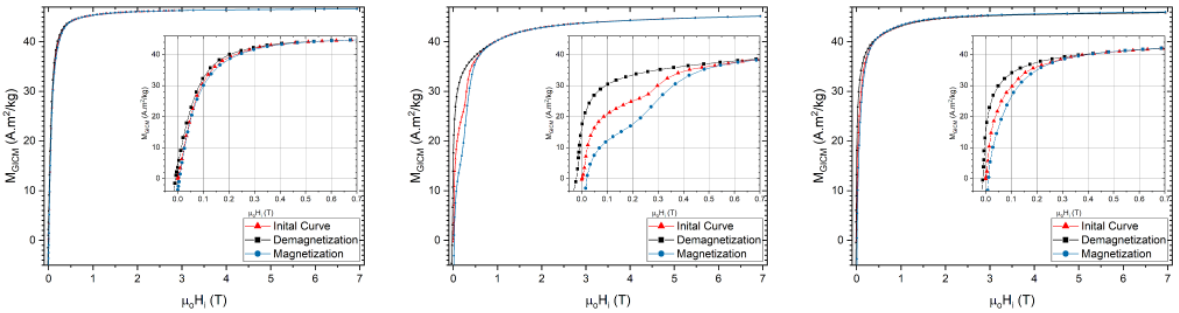

(a) $M(H)$ curves of the 1 hour and 30 min at 500 °C sample.

(b) $M(H)$ curves of the 2 hours at 500 °C sample.

(c) $M(H)$ curves of the 2 hours at 600 °C sample.

Figure 3.7: Comparison of the $M(H)$ curves measured at 10 K.

Calculating the areas of the different hysteresis of the curves measured at 10 K provides the information shown in figure 3.8. In this case, the 500 °C heat treatments have a similar trend to the one observed in the precipitates formation, while the heat treatments made at 600 °C have a more erratic progression, going up on the 1 hour at 600 °C and then going down for the 2 hour heat treatment. As a consequence, this measurement still falls short of the goal to provide a reliable source of information that could be used as an indicator of the precipitates formation.

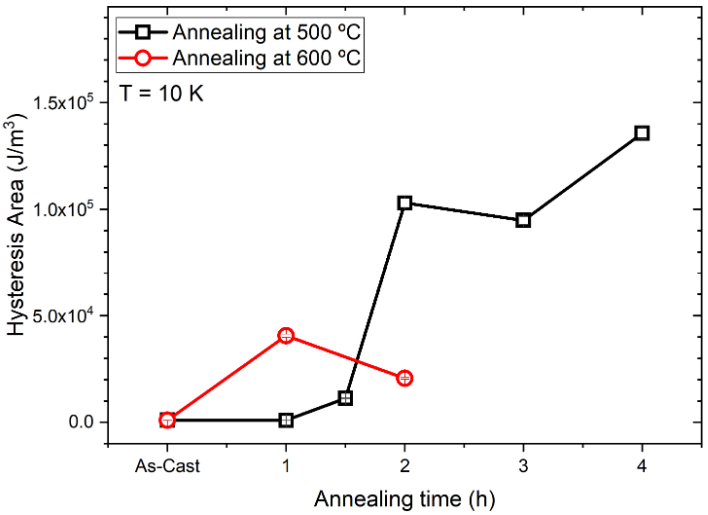

Figure 3.8: Magnetization hysteresis of the $M(H)$ curves measured at 10 K.

3.2.3 Influence of Precipitation on the Approach to Saturation

Using the process and tools described in subsection 2.3.2, it was found that the equation 2.4 provided very good fits across all the different heat treatments, especially on the heat treatments made at 500 °C with times longer than 2 hours. The term A_2/H_i, plays an important role, where without it, the residuals and the fit quality was impacted. The fact that this term also coincides with the defects and impurities [46] reported in literature, further adds consistency to the method and approach used. However, for a transparent analysis, it should be noted that there is some literature that refers that, depending on the type of precipitates, it might not be possible to detect them [50]. In this case, it is important to make some much

needed distinctions and put their results into context. On this theoretical calculation, it has been stated that in an amorphous matrix, the effects of the precipitates are very small and cannot be responsible for the experimentally observed term. Even so, in the case of the Co−Ni−Ga system, it is important to notice that these precipitates create complex stress fields in a crystalline matrix, which changes how the rotation of the magnetization proceeds towards the saturation magnetization [30], particularly on the martensite phase which has a distorted structure from the austenite one. As such, the result presented in this section can be interpreted as a defect that changes the stress field and is thus being detected by this term.

The other term, $\chi_0/M_s H_i$, included in equation 2.4, also plays a critical role at very high fields, and without it the residuals in these regions present big deviations from the ideal 0 value. Again, the literature also presents this term as high-field susceptibility [45, 48], which was verified on the curves of the heat treatments that were studied in this work.

After each term was obtained and plotted against it's respective heat treatment, the result is in figure 3.9a and 3.9b, for the terms A_2 and χ_0/M_s, respectively.

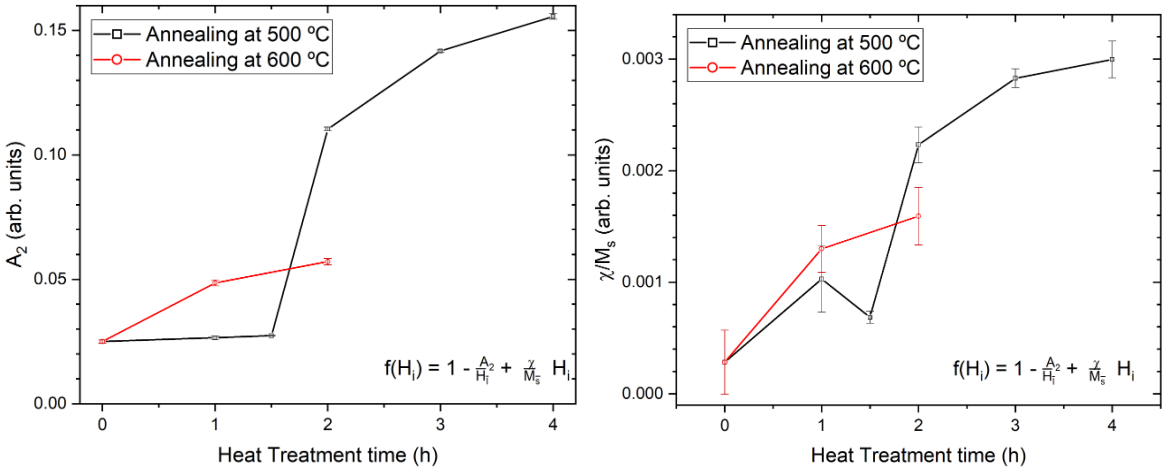

(a) Term A_2 of the equation 2.4 in function of the respective heat treatment.

(b) Term χ_0/M_s of the equation 2.4 in function of the respective heat treatment.

Figure 3.9: Plotting of each term of the fitting done to the initial curves of magnetization with equation 2.4. The initial curves used were the ones from the measurements done at 10 K.

Inspecting the results obtained in figure 3.9a it is possible to observe that the term A_2 matches with the precipitates growth trend. The characteristic of the heat treatments made at 500 °C having a slower start, but at the 2 hour having a sharp increase hereafter is also observed in the figure 3.1 of the precipitates formation. This slow start can indicate that the precipitates formed for those temperatures are being absorbed by the martensitic phase, due to their small size, and as such, do not create a high enough stress field to be detected. However, the fact that the heat treatment made at 2 hours at 500 °C is higher than the one made at 600 °C does not coincide with the quantification of the precipitates that it was hoped for, unless one considers the uncertainity on the area measurement of the precipitates. Nonetheless, is important to recall that this is not a direct comparison, and what this result shows is that the overall trend and growth is pretty much the same and, what is possibly

happening here, is the growth of different regimes of precipitates, that create different stress fields on the material, are being revealed by the Law of Approach to Saturation.

Interestingly, the second term of the equation, χ_0/M_s, presents a similar situation as the one observed on the term A_2, but it also presents the erratic behaviour for the 1 hour at 500 °C sample. The fitting for this heat treatment did not go as smoothly as the other ones and this reveals itself in the graph as having a higher error bar than the other heat treatments. Overall this term also shows some similarities to the trends of the growth of the precipitates. This term is described as the high-field susceptibility of the material.

For the most part, the Law of Approach to Saturation in the form of equation 2.4 fitted the data obtained very well, while the terms that were obtained can be used as an indicator of the type and amount of precipitates that are being formed.

CHAPTER 4

Conclusions

Concluding this work, some relevant information on the formation of the precipitates in the Co−Ni−Ga system was obtained. In this case, an extensive preparation of a range of heat treatments were made to study the precipitates that formed on the Co−Ni−Ga system in the polycrystalline state.

A systematic method using ImageJ and MatLab on the BSE images was created. It provided the necessary quantification of the area of the precipitates that were being formed, which was then used as baseline information to relate the magnetic characterization, as well as knowledge of the needle-like shape of the precipitates.

The analysis of the phase transitions temperatures, through the $M(T)$ curves, presented some challenges in the estimation and did not provide enough reliability to be used for the precipitates quantification. Even then, it allowed to verify that the precipitates do decrease these phase transitions temperatures for longer heat treatments, but it is still unclear of what is happening for the shorter heat treatments, in which the phase transitions temperatures seem to slightly increase. As such, there is now a question if, in fact, what is happening in this case is the formation of different precipitates for the different heat treatment temperatures.

The saturation magnetization, taken from the $M(H)$ curves, did not provide the insight that one was looking for. First, it is necessary to comprehend that the amount of austenite that has transformed to martensite is not the same in all of the samples. Second, the loss in magnetization of the matrix, caused by the movement of Co to the precipitates, most probably compensates the gain in magnetization made by the precipitates. The result is a net magnetization that follows the same trend seen in the precipitate formation, but the difference between the values is negligible, since the magnetization values are almost the same and within the uncertainty of each other.

The shape of the hysteresis provided some information about the dynamic behaviour of the magnetization of the precipitates, and supports the idea of different precipitates being formed. The calculation of the area of the hysteresis showed some progress towards the main goal of this work, but the trend shown by the heat treatments at 600 °C is not the one expected and

the situation of the uncertainty is similar to the one observed on the measurement of the saturation magnetization.

Finally, the Law of Approach to Saturation was applied to the $M(H)$ curves and it can be used as an indicator for the amount of precipitates, or the types of precipitates that are being formed. In this case, from the general equation with several terms, it was found that the most relevant terms are the ones present in equation 2.4, with the more relevant term being the A_2. These terms are sufficient for very good fits of all of the curves, and the curves of the 500 °C and 600 °C with precipitates are the ones that fit better. As such, when plotting the individual terms obtained from these fittings, it is possible to get a reasonable indicator of the amount and/or types of precipitates that are being formed.

References

1. Calkins, F. T. & Mabe, J. H. Shape memory alloy based morphing aerostructures (2010).

2. Nespoli, A., Besseghini, S., Pittaccio, S., Villa, E. & Viscuso, S. The high potential of shape memory alloys in developing miniature mechanical devices: A review on shape memory alloy mini-actuators. *Sensors and Actuators A: Physical* **158,** 149–160 (2010).

3. Petrini, L. & Migliavacca, F. Biomedical applications of shape memory alloys. *Journal of Metallurgy* **2011** (2011).

4. Lagoudas, D. C. *Shape memory alloys: modeling and engineering applications* (Springer, 2008).

5. Buehler, W. J., Gilfrich, J. V. & Wiley, R. Effect of low-temperature phase changes on the mechanical properties of alloys near composition TiNi. *Journal of applied physics* **34,** 1475–1477 (1963).

6. Wuttig, M., Li, J. & Craciunescu, C. A new ferromagnetic shape memory alloy system. *Scripta materialia* **44,** 2393–2397 (2001).

7. Liu, J., Zheng, H., Xia, M., Huang, Y. & Li, J. Martensitic transformation and magnetic properties in Heusler CoNiGa magnetic shape memory alloys. *Scripta materialia* **52,** 935–938 (2005).

8. Oikawa, K. *et al.* Phase equilibria and phase transformation of Co- Ni- Ga ferromagnetic shape memory alloy system. *Journal of Phase Equilibria and Diffusion* **27,** 75–82 (2006).

9. Otsuka, K. & Wayman, C. M. *Shape memory materials* (Cambridge university press, 1999).

10. Dadda, J., Maier, H., Karaman, I., Karaca, H. & Chumlyakov, Y. I. Pseudoelasticity at elevated temperatures in [0 0 1] oriented Co49Ni21Ga30 single crystals under compression. *Scripta materialia* **55,** 663–666 (2006).

11. Liu, J., Xie, H., Huo, Y., Zheng, H. & Li, J. Microstructure evolution in CoNiGa shape memory alloys. *Journal of alloys and compounds* **420,** 145–157 (2006).

12. Seo, J., Kim, Y. C. & Hu, J. W. Pilot study for investigating the cyclic behavior of slit damper systems with recentering shape memory alloy (SMA) bending bars used for seismic restrainers. *Applied Sciences* **5,** 187–208 (2015).

13. Chernenko, V. & Besseghini, S. Ferromagnetic shape memory alloys: Scientific and applied aspects. *Sensors and Actuators A: Physical* **142,** 542–548 (2008).

14. Firstov, G., Van Humbeeck, J. & Koval, Y. N. High-temperature shape memory alloys: some recent developments. *Materials Science and Engineering: A* **378,** 2–10 (2004).

15. Ma, J., Karaman, I. & Noebe, R. D. High temperature shape memory alloys. *International Materials Reviews* **55,** 257–315 (2010).

16. Karaca, H., Karaman, I., Lagoudas, D., Maier, H. & Chumlyakov, Y. I. Recoverable stress-induced martensitic transformation in a ferromagnetic CoNiAl alloy. *Scripta materialia* **49,** 831–836 (2003).

17. Dogan, E., Karaman, I., Chumlyakov, Y. I. & Luo, Z. Microstructure and martensitic transformation characteristics of CoNiGa high temperature shape memory alloys. *Acta materialia* **59,** 1168–1183 (2011).

18. Van Humbeeck, J. High temperature shape memory alloys (1999).

19. Elahinia, M. H., Hashemi, M., Tabesh, M. & Bhaduri, S. B. Manufacturing and processing of NiTi implants: A review. *Progress in materials science* **57,** 911–946 (2012).

20. Sozinov, A., Likhachev, A. & Ullakko, K. Crystal structures and magnetic anisotropy properties of Ni-Mn-Ga martensitic phases with giant magnetic-field-induced strain. *IEEE transactions on magnetics* **38,** 2814–2816 (2002).

21. Ma, Y.-Q., Jiang, C.-B., Feng, G. & Xu, H. Thermal stability of the Ni54Mn25Ga21 Heusler alloy with high temperature transformation. *Scripta Materialia* **48,** 365–369 (2003).

22. Huang, W. On the selection of shape memory alloys for actuators. *Materials & design* **23,** 11–19 (2002).

23. Oikawa, K. *et al.* Phase equilibria and phase transformations in new B2-type ferromagnetic shape memory alloys of Co–Ni–Ga and Co–Ni–Al systems. *Materials transactions* **42,** 2472–2475 (2001).

24. Ullakko, K., Huang, J., Kantner, C., O'handley, R. & Kokorin, V. Large magnetic-field-induced strains in Ni2MnGa single crystals. *Applied Physics Letters* **69,** 1966–1968 (1996).

25. Sozinov, A., Likhachev, A., Lanska, N. & Ullakko, K. Giant magnetic-field-induced strain in NiMnGa seven-layered martensitic phase. *Applied Physics Letters* **80,** 1746–1748 (2002).

26. Sato, M., Okazaki, T., Furuya, Y. & Wuttig, M. Magnetostrictive and shape memory properties of Heusler type Co_2NiGa alloys. *Materials Transactions* **44,** 372–376 (2003).

27. Dadda, J. *et al.* Stress–strain–temperature behaviour of [001] single crystals of Co49Ni21Ga30 ferromagnetic shape memory alloy under compression. *Philosophical Magazine* **87,** 2313–2322 (2007).

28. Prusik, K. *et al.* The effect of γ-phase particles on microstructure and properties of Co–Ni–Ga alloys. *The European Physical Journal Special Topics* **158,** 155–159 (2008).

29. Liu, J., Xia, M., Huang, Y., Zheng, H. & Li, J. Effect of annealing on the microstructure and martensitic transformation of magnetic shape memory alloys CoNiGa. *Journal of alloys and compounds* **417,** 96–99 (2006).

30. Kireeva, I. *et al.* Effect of oriented γ' precipitates on shape memory effect and superelasticity in Co–Ni–Ga single crystals. *Acta materialia* **68,** 127–139 (2014).

31. Lauhoff, C. *et al.* Pathways towards grain boundary engineering for improved structural performance in polycrystalline Co–Ni–Ga shape memory alloys. *Shape Memory and Superelasticity* **5,** 73–83 (2019).

32. Vollmer, M. *et al.* Damage evolution in pseudoelastic polycrystalline Co–Ni–Ga high-temperature shape memory alloys. *Journal of Alloys and Compounds* **633,** 288–295 (2015).

33. Kireeva, I. *et al.* Influence of γ' nanometric particles on martensitic transformation and twinning structure of $L1_0$ martensite in Co–Ni–Ga ferromagnetic shape memory single crystals. *Intermetallics* **35,** 60–66 (2013).

34. Chernenko, V. Compositional instability of β-phase in Ni-Mn-Ga alloys. *Scripta Materialia* **40,** 523–527 (1999).

35. Chumlyakov, Y. I., Kireeva, I., Kretinina, I. & Kirillov, V. Peculiarities of thermoelastic martensite transformations under loading in CoNiGa single crystals with different number of variants of γ'-phase particles. *Russian Physics Journal* **55,** 1290–1295 (2013).

36. Li, Y. *et al.* Magnetic field-controlled two-way shape memory in CoNiGa single crystals. *Applied physics letters* **84,** 3594–3596 (2004).

37. Scheibel, F. *et al.* On the impact of additive manufacturing processes on the microstructure and magnetic properties of Co–Ni–Ga Shape Memory Heusler alloys. *Advanced Engineering Materials,* 2200069 (2022).

38. Melting, V. I. ASM Handbook 2008, Volume 15: Casting. *Handbook Committee,* 1–8.

39. Ltd., J. *3-1-2 Musashino, Akishima, Tokyo 196-8558, JAPAN* `https://www.jeol.co.jp/en/products/detail/JSM-7600F.html`.

40. Inc., Q. D. *10307 Pacific Center Court, San Diego, CA 92121, USA* `https://www.qdusa.com/index.html`.

41. Buchner, M., Höfler, K., Henne, B., Ney, V. & Ney, A. Tutorial: Basic principles, limits of detection, and pitfalls of highly sensitive SQUID magnetometry for nanomagnetism and spintronics. *Journal of Applied Physics* **124,** 161101 (2018).

42. Fagaly, R. Superconducting quantum interference device instruments and applications. *Review of scientific instruments* **77,** 101101 (2006).

43. Inc., Q. D. *Magnetic Property Measurement System - MPMS3 User's Manual* (2016).

44. Amorim, C., Mohseni, F., Dumas, R., Amaral, V. & Amaral, J. A geometry-independent moment correction method for the MPMS3 SQUID-based magnetometer. *Measurement Science and Technology* **32,** 105602 (2021).

45. Chikazumi, S., Chikazumi, S. & Graham, C. D. *Physics of ferromagnetism* **94** (Oxford University Press, 1997).

46. Umetsu, R. *et al.* Effects of the antiferromagnetic anti-phase domain boundary on the magnetization processes in Ni2Mn(Ga0.5Al0.5) Heusler alloy. *Scripta Materialia* **65,** 41–44 (2011).

47. Andreev, S. *et al.* Law of approach to saturation in highly anisotropic ferromagnets Application to Nd-Fe-B melt-spun ribbons. *Journal of alloys and compounds* **260,** 196–200 (1997).

48. Groessinger, R. A critical examination of the law of approach to saturation. I. Fit procedure. *physica status solidi (a)* **66,** 665–674 (1981).

49. Sobrero, C. *et al.* γ-phase evolution in aged Co−Ni−Ga shape memory alloy. *Functional Materials Letters* **15,** 2250007 (2022).

50. Fähnle, M. The influence of precipitates on the law of approach to magnetic saturation in amorphous ferromagnets. *Journal of Magnetism and Magnetic Materials* **8,** 257–258 (1978).

Appendix A - Scanning Electron Microscopy Imaging

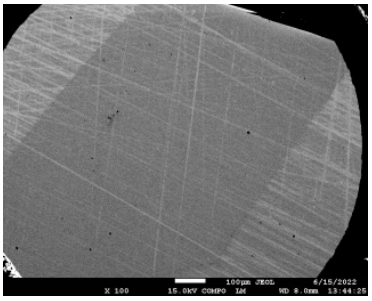

(a) Amplification of 100x.

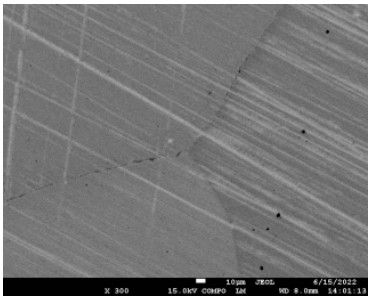

(b) Amplification of 300x.

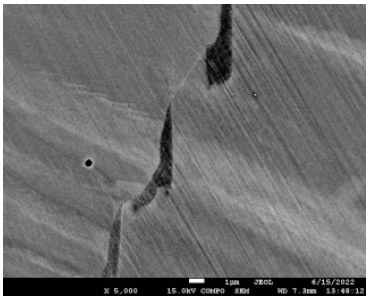

(c) Amplification of 5000x.

Figure 1: SEM images of the As-Cast sample.

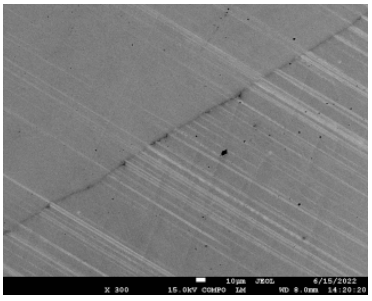

(a) Amplification of 300x.

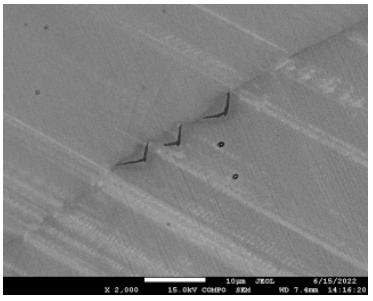

(b) Amplification of 2000x.

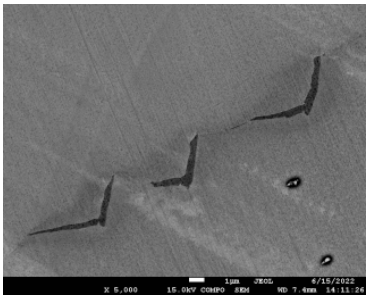

(c) Amplification of 5000x.

Figure 2: SEM images of the 1 hour at 400 °C sample.

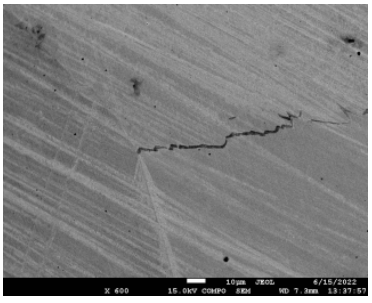

(a) Amplification of 600x.

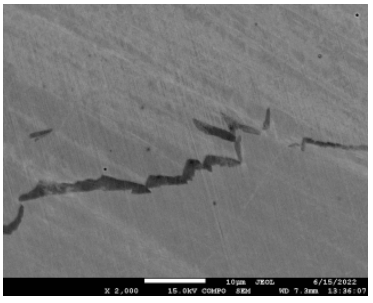

(b) Amplification of 2000x.

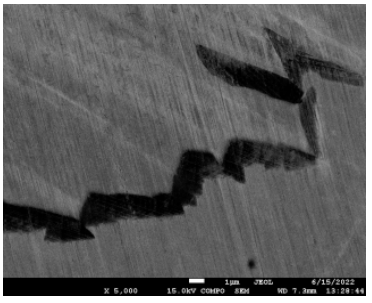

(c) Amplification of 5000x.

Figure 3: SEM images of the 1 hour at 500 °C sample.

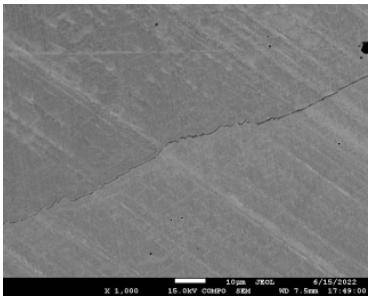

(a) Amplification of 600x.

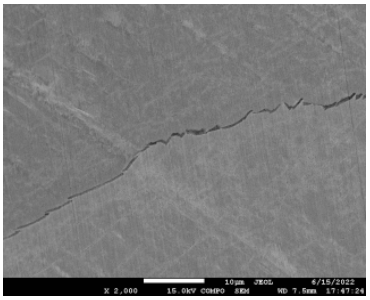

(b) Amplification of 2000x.

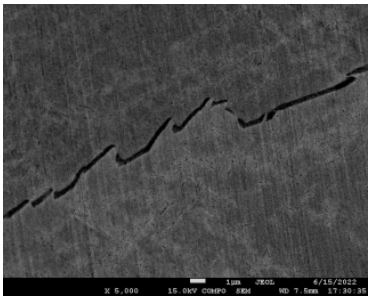

(c) Amplification of 5000x.

Figure 4: SEM images of the 1 hour and 30 min at 500 °C sample.

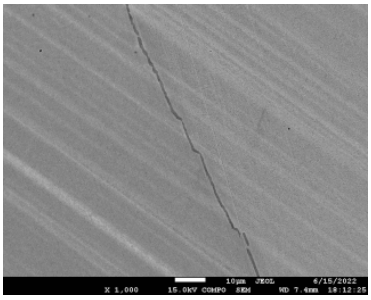

(a) Amplification of 1000x.

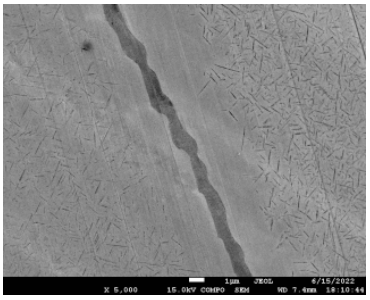

(b) Amplification of 5000x.

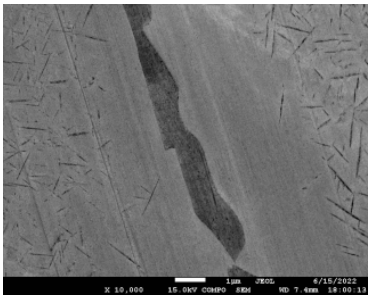

(c) Amplification of 10000x.

Figure 5: SEM images of the 2 hours at 500 °C sample.

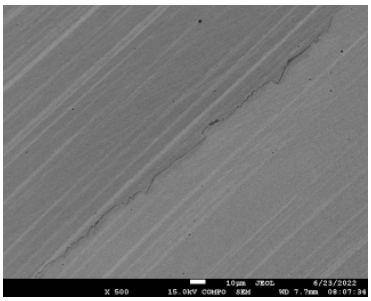

(a) Amplification of 500x.

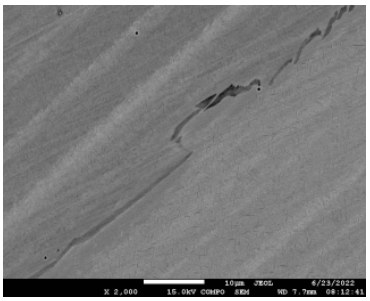

(b) Amplification of 2000x.

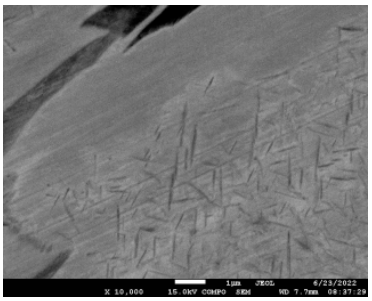

(c) Amplification of 10000x.

Figure 6: SEM images of the 3 hours at 500 °C sample.

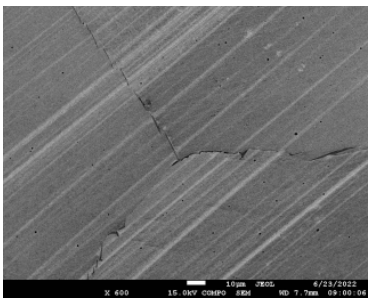

(a) Amplification of 600x.

(b) Amplification of 5000x.

(c) Amplification of 10000x.

Figure 7: SEM images of the 4 hours at 500 °C sample.

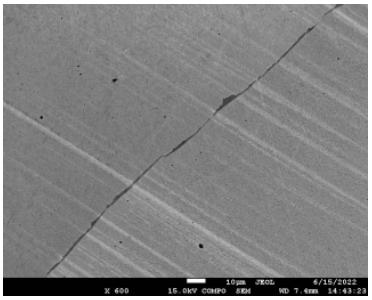

(a) Amplification of 600x.

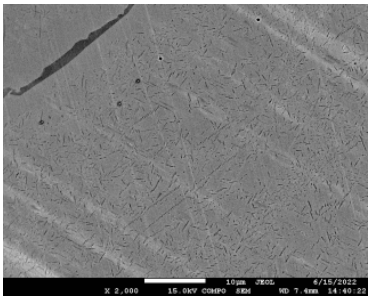

(b) Amplification of 2000x.

(c) Amplification of 5000x.

Figure 8: SEM images of the 1 hour at 600 °C sample.

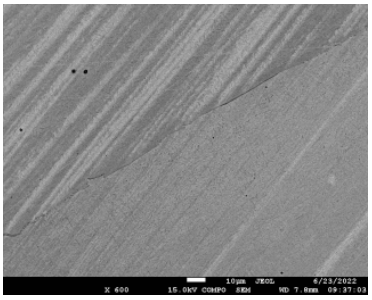

(a) Amplification of 600x.

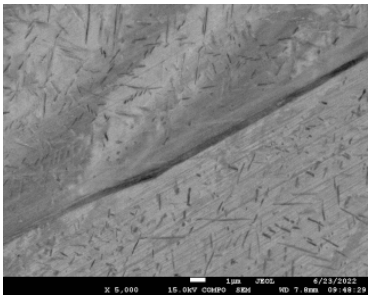

(b) Amplification of 5000x.

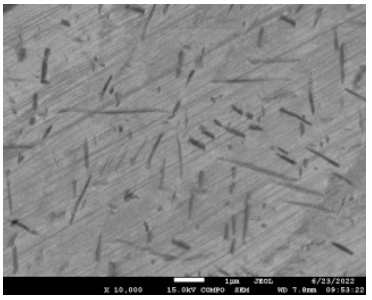

(c) Amplification of 10000x.

Figure 9: SEM images of the 2 hours at 600 °C sample.

Appendix B - Precipitates Analysis

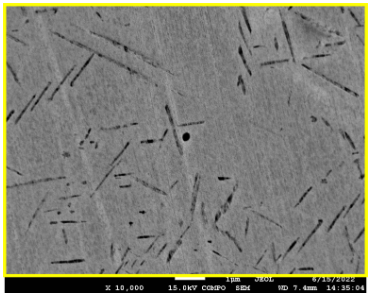

(a) Area selection for the 1 hour at 600 °C sample.

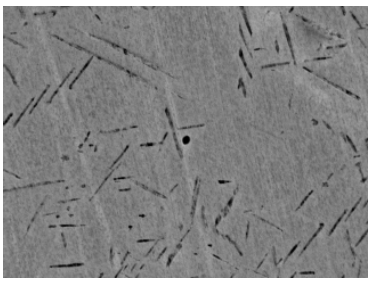

(b) Baseline image of the selection of 1 hour at 600 °C sample.

(c) High contrast image of 1 hour at 600 °C sample.

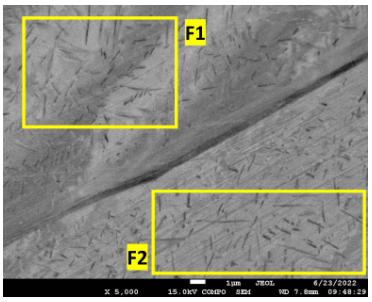

(d) Area selection for the 2 hours at 600 °C sample.

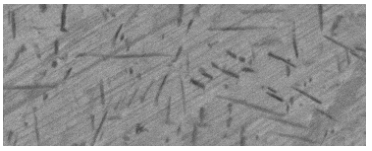

(e) Baseline image of the selection of 2 hours at 600 °C sample.

(f) High contrast image of 2 hours at 600 °C sample.

Figure 10: Process and selection of the images used on the calculation of the area of the precipitates for each of the annealings done.

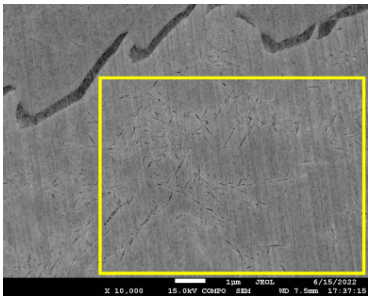

(a) Area selection for the 1 hour and 30 min at 500 °C sample.

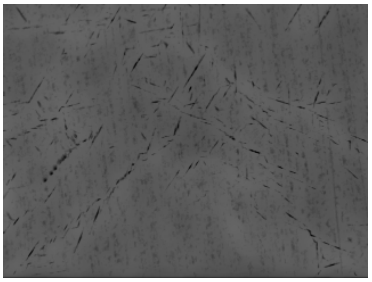

(b) Baseline image of the selection of 1 hour and 30 min at 500 °C sample.

(c) High contrast image of 1 hour and 30 min at 500 °C sample.

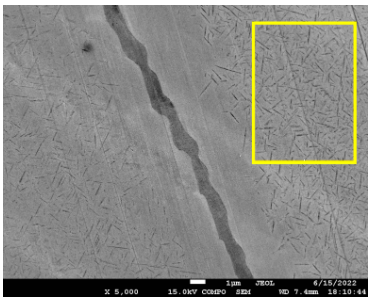

(d) Area selection for the 2 hours at 500 °C sample.

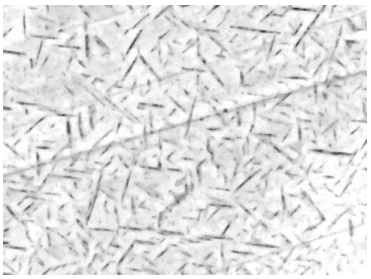

(e) Baseline image of the selection of 2 hours at 500 °C sample.

(f) High contrast image of 2 hours at 500 °C sample.

(g) Area selection for the 3 hours at 500 °C sample.

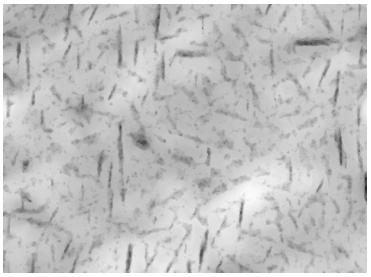

(h) Baseline image of the selection of 3 hours at 500 °C sample.

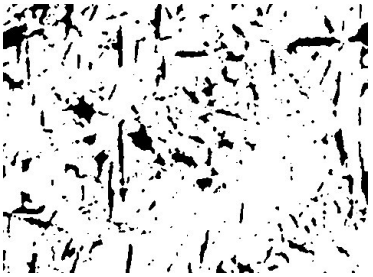

(i) High contrast image of 3 hours at 500 °C sample.

(j) Area selection for the 4 hours at 500 °C sample.

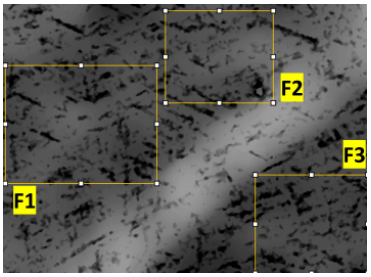

(k) Baseline image of the selections of the 4 hours at 500 °C sample

(l) High contrast image of 4 hours at 500 °C sample, the F1 area.

Figure 11: Process and selection of the images used on the calculation of the area of the precipitates for each of the annealings done.

Appendix C - Magnetization with field and temperature dependence

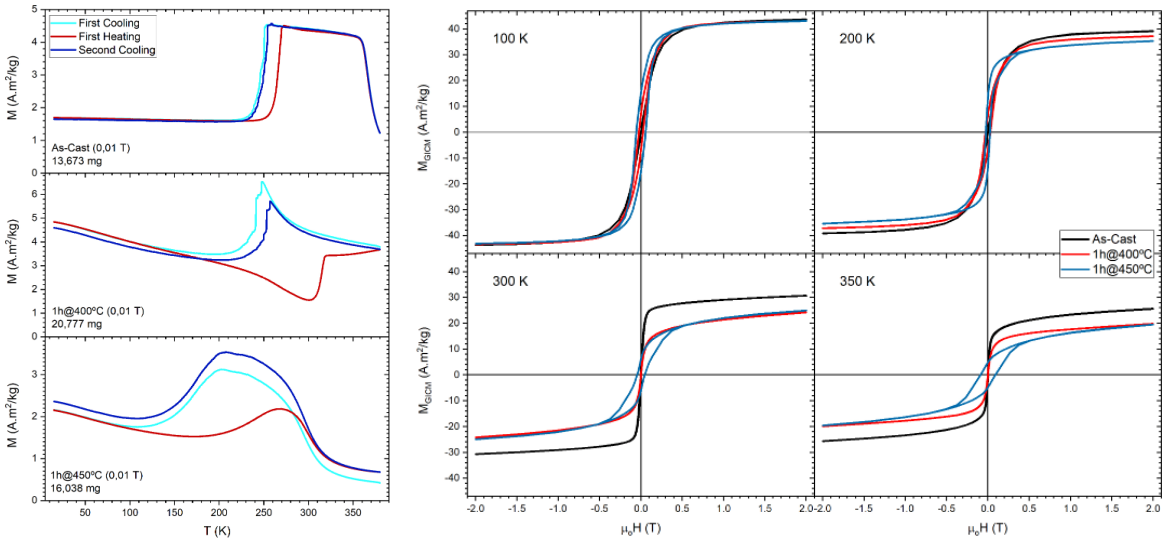

(a) Magnetization in function of temperature.

(b) Magnetization in function of applied field.

Figure 12: Comparison of the M(T) and M(H) curves of the As-Cast, 1 hour at 400 °C and 1 hour at 450 °C samples.

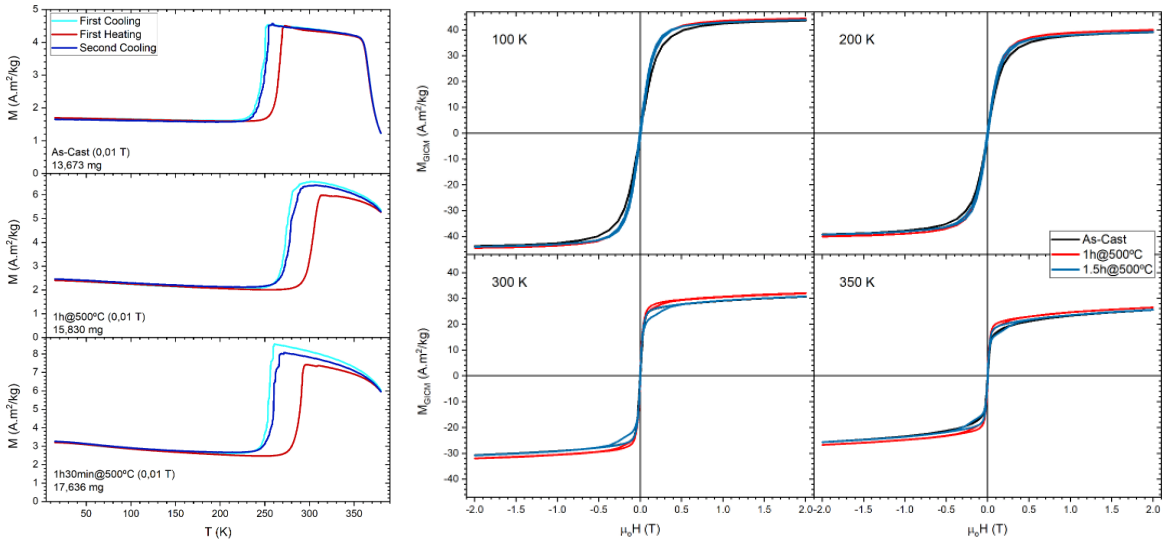

(a) Magnetization in function of temperature.

(b) Magnetization in function of applied field.

Figure 13: Comparison of the M(T) and M(H) curves of the Non Heat Treated, 1 hour at 400 °C and 1 hour at 450 °C samples.

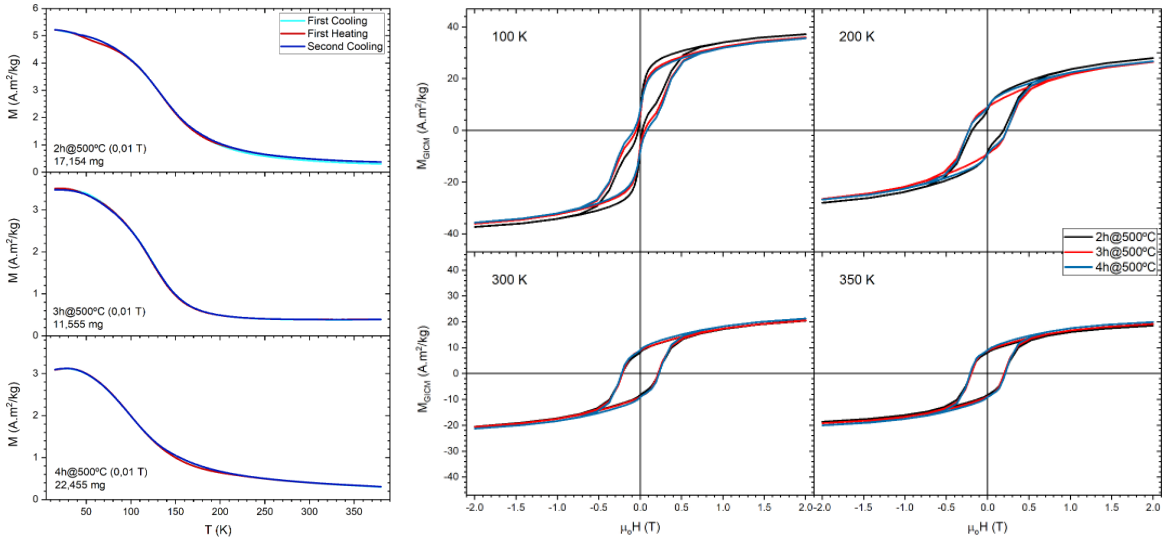

(a) Magnetization in function of temperature.

(b) Magnetization in function of applied field.

Figure 14: Comparison of the M(T) and M(H) curves of the 2 hours at 500 °C, 3 hours at 500 °C and 4 hours at 500 °C samples.

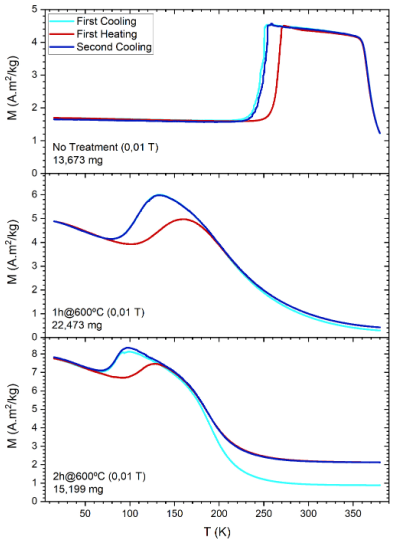

(a) Magnetization in function of temperature.

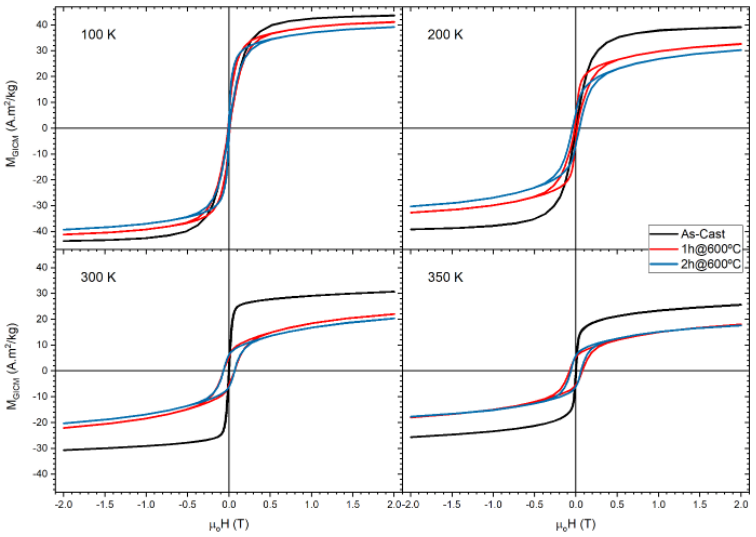

(b) Magnetization in function of applied field.

Figure 15: Comparison of the M(T) and M(H) curves of the No Treatment , 1 hour at 600 °C and 2 hours at 600 °C samples.

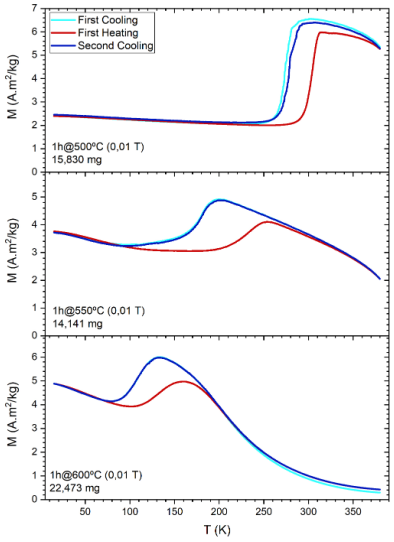

(a) Magnetization in function of temperature.

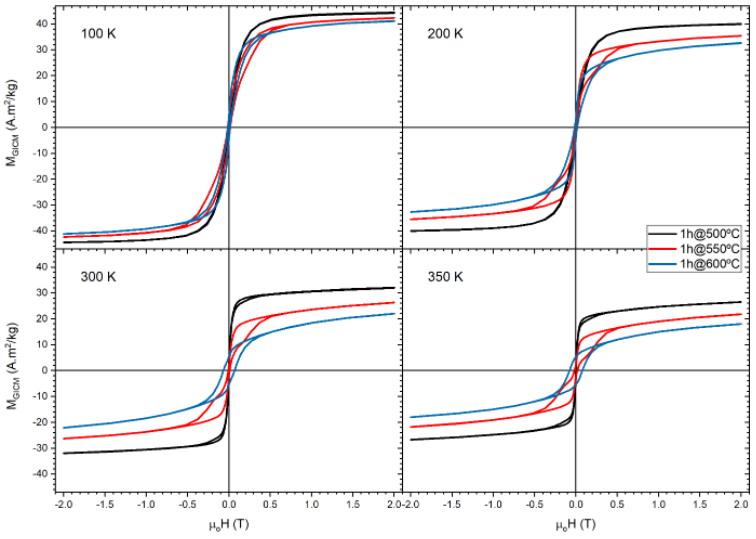

(b) Magnetization in function of applied field.

Figure 16: Comparison of the M(T) and M(H) curves of the 1 hour at 500 °C, 1 hour at 550 °C and 1 hour at 600 °C samples.

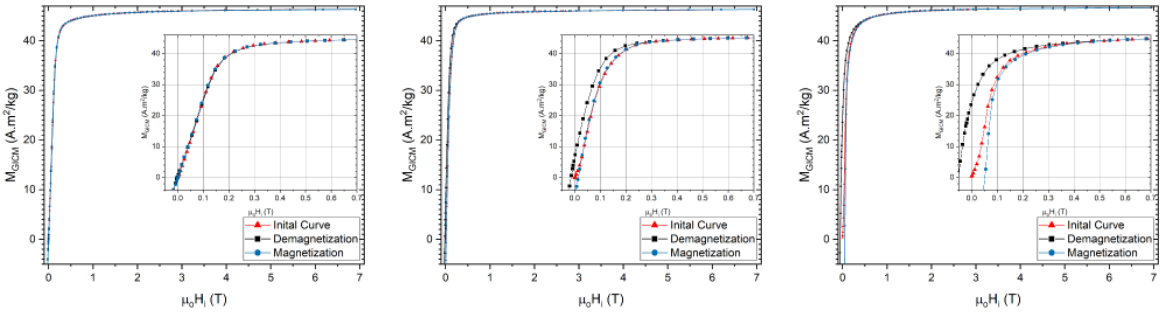

(a) As-Cast sample. **(b)** 1 hour at 400 °C sample. **(c)** 1 hour at 450 °C sample.

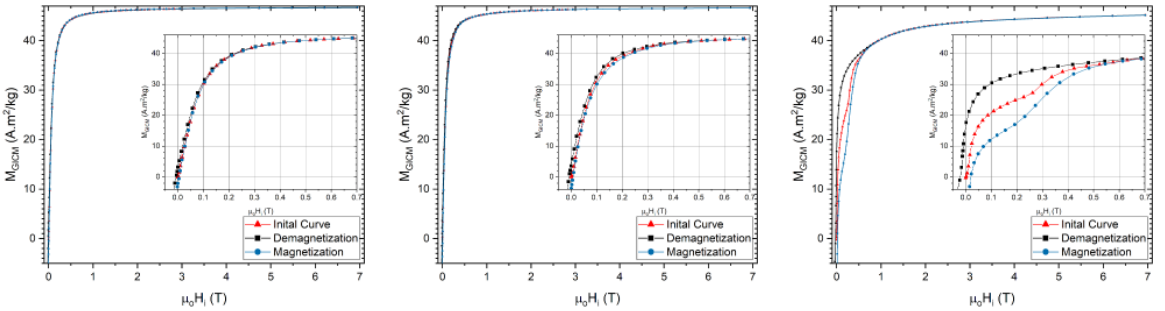

(d) 1 hour at 500 °C sample. **(e)** 1 hour and 30 min at 500 °C sample. **(f)** 2 hours at 500 °C sample.

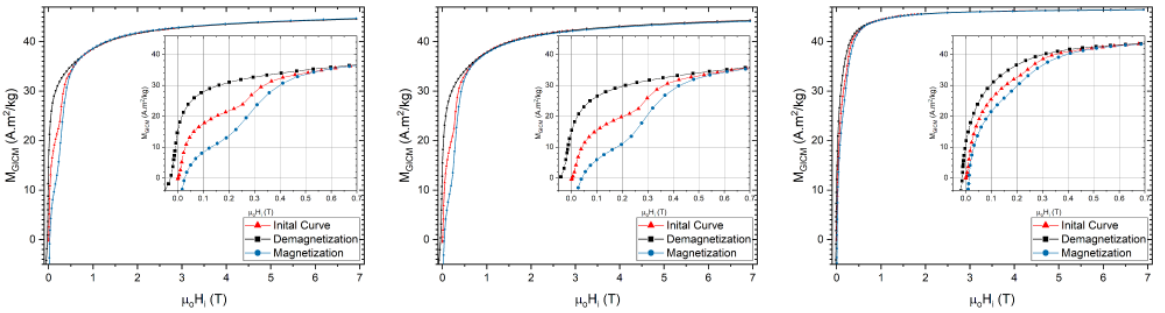

(g) 3 hours at 500 °C sample. **(h)** 4 hours at 500 °C sample. **(i)** 1 hour at 550 °C sample.

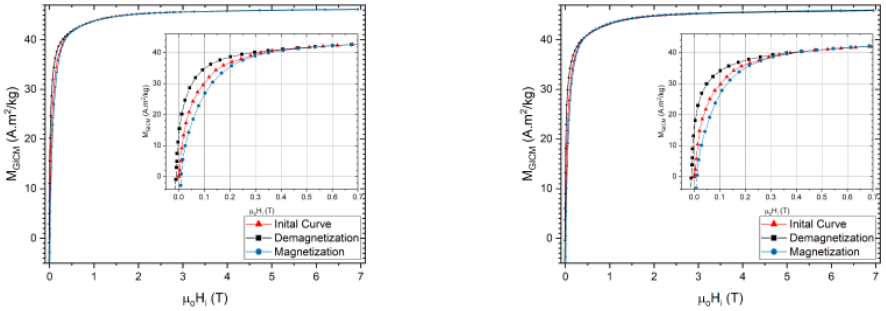

(j) 1 hour at 600 °C sample. **(k)** 2 hours at 600 °C sample.

Figure 17: Magnetization in function of applied field measured at 10 K.

Appendix D - Law Of Approach to Saturation

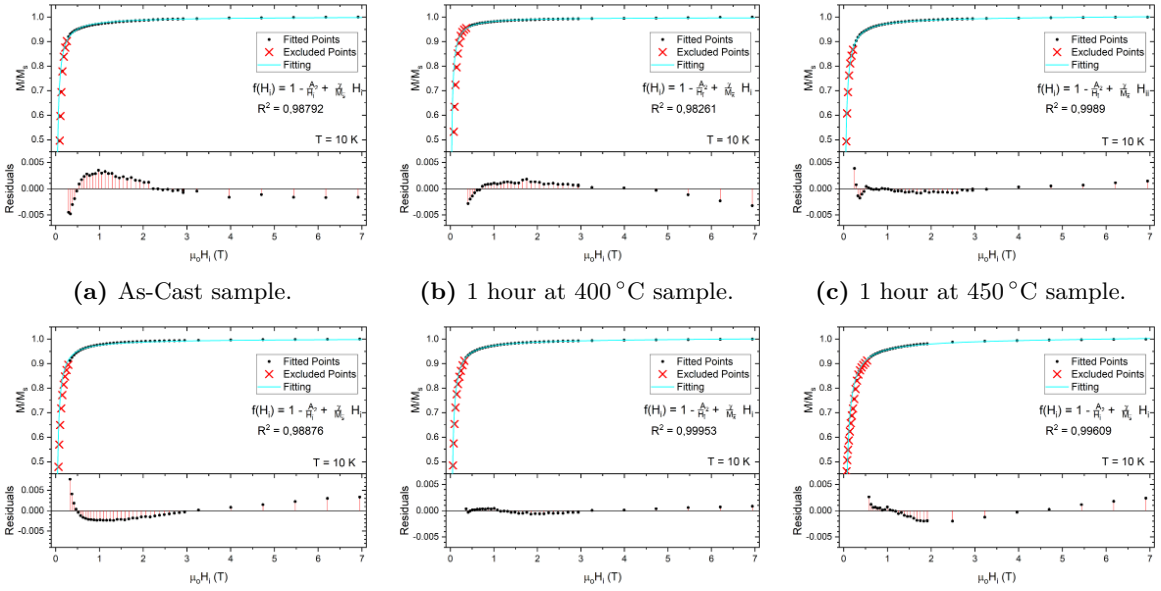

(a) As-Cast sample. **(b)** 1 hour at 400 °C sample. **(c)** 1 hour at 450 °C sample.

(d) 1 hour at 500 °C sample. **(e)** 1 hour and 30 min at 500 °C sample. **(f)** 1 hour at 550 °C sample.

Figure 18: Fitting of the Law of Approach to Saturation to the initial magnetization at 10 K.

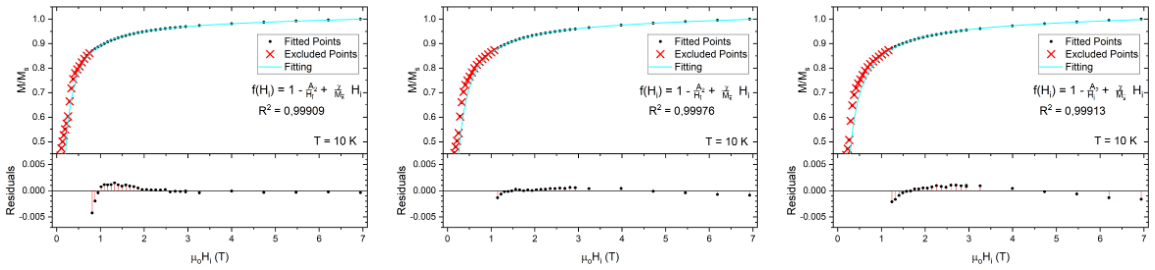

(a) 2 hours at 500 °C sample. **(b)** 3 hours at 500 °C sample. **(c)** 4 hours at 500 °C sample.

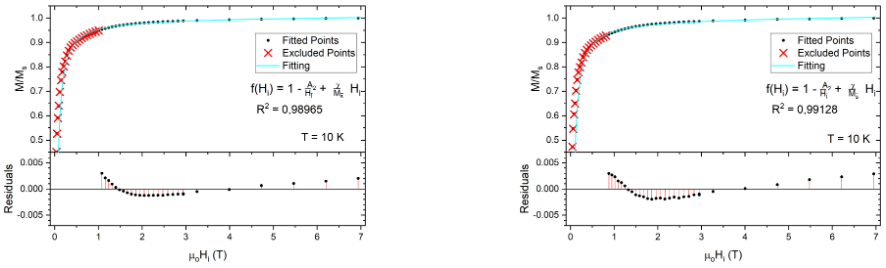

(d) 1 hour at 600 °C sample. **(e)** 2 hours at 600 °C sample.

Figure 19: Fitting of the Law of Approach to Saturation to the initial magnetization at 10 K.